

Fast multiplexed superconducting qubit readout with intrinsic Purcell filtering

Peter A. Spring,^{1,*} Luka Milanovic,^{1,2} Yoshiki Sunada,^{1,3} Shiyu Wang,¹

Arjan F. van Loo,^{1,4} Shuhei Tamate,¹ and Yasunobu Nakamura^{1,4}

¹*RIKEN Center for Quantum Computing (RQC), Wako, Saitama 351-0198, Japan*

²*Department of Physics, ETH Zürich, Otto-Stern-Weg 1, 8093 Zürich, Switzerland*

³*QCD Labs, QTF Centre of Excellence, Department of Applied Physics, Aalto University, P.O. Box 13500, FIN-00076 Aalto, Finland*

⁴*Department of Applied Physics, Graduate School of Engineering, The University of Tokyo, Bunkyo-ku, Tokyo 113-8656, Japan*

(Dated: September 12, 2024)

Fast and accurate qubit measurement remains a critical challenge on the path to fault-tolerant quantum computing. In superconducting quantum circuits, fast qubit measurement has been achieved using a dispersively coupled resonator with a large external linewidth. This necessitates the use of a Purcell filter that protects the qubit from relaxation through the readout channel. Here we show that a readout resonator and filter resonator, coupled to each other both capacitively and inductively, can produce a compact notch-filter circuit that effectively eliminates the Purcell decay channel through destructive interference. By utilizing linewidths as large as 42 MHz, we perform 56-ns simultaneous readout of four qubits and benchmark an average assignment fidelity of 99.77%, with the highest qubit assignment fidelity exceeding 99.9%. These results demonstrate a significant advancement in speed and fidelity for multiplexed superconducting qubit readout.

I. INTRODUCTION

Quantum computing relies on the accurate measurement of qubit states. In superconducting quantum circuits, measurement now constitutes a major component of the error budget for algorithms requiring detection and feedback. This is significant for the execution of quantum error correction codes such as the surface code [1–6], which require the measurement of ancilla qubits at the end of every error-correction cycle. It is equally important in measurement-based protocols for preparing entangled states [7–11] and performing long-range entangling gates [12], where unitary qubit operations are replaced by mid-circuit measurements and dynamical feedback.

Fast superconducting qubit readout has been achieved by dispersively coupling qubits to readout resonators that possess large external linewidths [13–17]. By further inserting a dedicated filter resonator between each readout resonator and the readout line [15], it is possible to suppress the Purcell relaxation channel and to reduce measurement crosstalk simultaneously.

However, as readout resonators with very large effective external linewidths are explored [18] and as energy relaxation times of superconducting qubits continue to improve well beyond 100 μ s [19–25], the Purcell filtering in circuits employing filter resonators may be insufficient to ensure that the Purcell relaxation channel remains adequately suppressed. This motivates the design of filter resonators with an auxiliary Purcell filtering mechanism.

An attractive approach to improve Purcell filtering is to engineer an ‘intrinsic’ filter that leverages properties

of the circuit to enhance the filtering without the need for additional circuit components. Example intrinsic filtering mechanisms have involved exploiting symmetry in the qubit [26–28], making use of a stray capacitance in the readout circuit [29], and utilizing the distributed nature of the readout resonator [16] and the readout feedline [30].

Here, we propose and experimentally demonstrate a readout-resonator and dedicated-filter configuration featuring an intrinsic notch-type filter. This is achieved by coupling two quarter-wavelength ($\lambda/4$) coplanar waveguide (CPW) resonators together through a multiconductor transmission line (MTL) [31], which is formed by bringing a segment of the resonator lines into close proximity. The capacitive and inductive interactions in the MTL destructively interfere, resulting in a notch frequency where signals cannot propagate through the resonators. We experimentally demonstrate that this filtering mechanism can effectively eliminate the Purcell relaxation channel when the notch is tuned to the qubit frequency. By utilizing readout modes with large effective linewidths, we then perform frequency-multiplexed readout of four qubits using a sub-60-ns measurement pulse and integration window, with the highest qubit assignment fidelity exceeding 99.9%.

The paper is organized as follows: First, a distributed-circuit model and an equivalent lumped-element circuit model for the coupled resonators are presented and utilized to find symbolic expressions for the notch frequency and the coupling strength between the resonators. Next, the notch filtering is experimentally demonstrated and the predictions of the symbolic formulas are verified. Finally, fast four-to-one multiplexed readout is characterized in a device featuring readout and filter resonators with intrinsic notch filtering.

* peter.spring@riken.jp

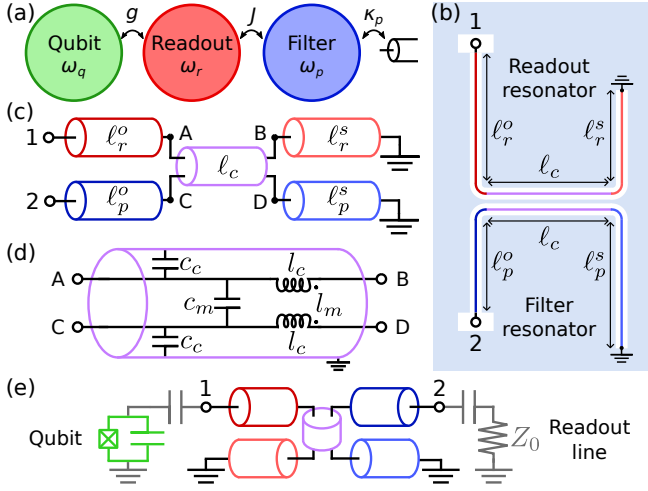


FIG. 1. Readout resonator and filter resonator with auxiliary notch filtering. (a) General arrangement of dispersive readout with a readout resonator and dedicated filter. (b) CPW configuration used in this work to construct a readout resonator and filter resonator with auxiliary notch filtering. (c) Distributed-circuit-model representation. The coupled section is treated as a MTL with two coupled lines. (d) Model of the MTL with the per-length parameters defined. (e) Depiction of a qubit coupled to the readout line through the distributed readout- and filter-resonator circuits.

II. MODEL

The general configuration of dispersive readout with a dedicated filter resonator is shown in Fig. 1(a). A qubit is dispersively coupled to a readout resonator with coupling strength g , which in turn is coupled to a filter resonator with coupling strength J . The filter resonator is then coupled to a readout line with an external linewidth of κ_p . Generally, it is advantageous to minimize the detuning between the readout resonator and filter resonator such that $|\omega_r - \omega_p| \ll J$ in order to maximize the rate at which incident readout photons acquire information about the qubit state [17, 32].

Figure 1(b) introduces the readout- and filter-resonator configuration used here to realize intrinsic notch filtering. Two $\lambda/4$ CPW resonators having characteristic impedance Z_0 and phase velocity v are coupled together through a length- ℓ_c section where the lines are brought into close proximity. The total lengths of the readout and filter resonators are $\ell_r = \ell_r^o + \ell_c + \ell_r^s$ and $\ell_p = \ell_p^o + \ell_c + \ell_p^s$, respectively, and their fundamental $\lambda/4$ resonances are at $\omega_{r(p)} = \pi v / (2\ell_{r(p)})$. As depicted in the figure, $\ell_{r(p)}^o$ ($\ell_{r(p)}^s$) denotes the lengths of line spanning between the open(shorted) end of each resonator and the coupled section.

Figure 1(c) presents the distributed circuit used to model the coupled resonators. The length- ℓ_c region where the coupling occurs is treated as an MTL with parameters defined in Fig. 1(d). The two lines of the MTL are coupled together by capacitance and inductance per

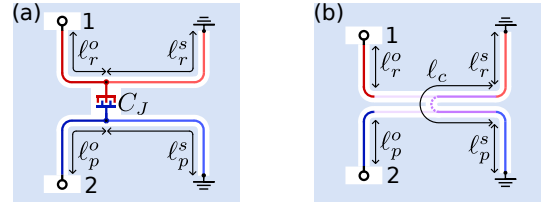


FIG. 2. Schematics of coupled $\lambda/4$ CPW resonators. (a) Diagram of lumped-element capacitive coupling between a pair of $\lambda/4$ resonators. (b) Geometric interpretation of the intrinsic notch that arises between a pair of MTL-coupled $\lambda/4$ resonators. The notch occurs at the anti-resonance frequency of the effective $\lambda/2$ resonator formed between the two resonators having a total length of $\ell_r^s + \ell_c + \ell_p^s$.

length, c_m and l_m , respectively. Both lines are symmetric with the same capacitance-to-ground and self-inductance per length, c_c and l_c , respectively.

By making appropriate assumptions about the MTL section, a symbolic expression for the transfer impedance $Z_{21}(\omega) \equiv V_2(\omega)/I_1(\omega)|_{I_2=0}$ between the two ports at the open ends of both resonators is derived [see Eq. (B7) in Appendix B]. At frequencies where $Z_{21} = 0$, the qubit in Fig. 1(e) is decoupled from the readout line because no amount of excitation applied at port 1 of the readout resonator can induce a voltage at port 2 of the filter resonator. Using this general solution, we proceed to analyze the behavior of the two resonators in the cases they are capacitively and MTL coupled. The capacitive coupling case serves as a reference in order to quantify the enhancement in Purcell filtering achieved through MTL coupling.

A. Capacitive coupling

Capacitive interaction between two $\lambda/4$ CPW resonators, i.e., a readout resonator and filter resonator, as depicted in Fig. 2(a) has been widely used for superconducting qubit readout [4, 5, 15, 17, 33]. A lumped-element capacitor represents a special case of the MTL depicted in Fig. 1(d), corresponding to the limits $c_m \ell_c \rightarrow C_J$ and $l_m, \ell_c \rightarrow 0$. In this case, the solution to $Z_{21}(\omega)$ [Eq. (B8) in Appendix B] has its first zero at a frequency greater than or equal to $\min(2\omega_r, 2\omega_p)$, confirming that it is not possible to engineer a notch filter in the relevant frequency range for Purcell filtering by using a purely capacitive coupling.

B. MTL coupling

Coupled CPWs on a substrate with permittivity ϵ_r behave to a good approximation as if they were embedded in a homogeneous medium with an effective permittivity of $\epsilon_{\text{eff}} = (1 + \epsilon_r)/2$ [34]. By applying this result to the MTL that couples the resonators, the solution to $Z_{21}(\omega)$

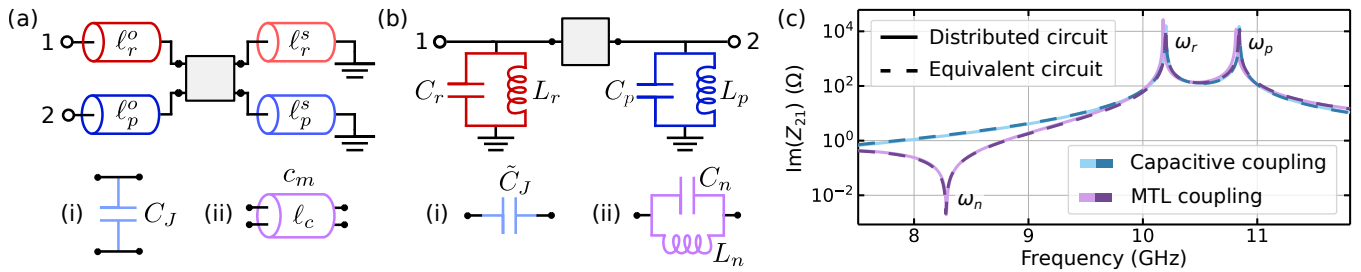


FIG. 3. (a) Distributed-circuit model for the coupled $\lambda/4$ resonators. The coupling element (gray square) represents (i) a lumped capacitor or (ii) a MTL. (b) Equivalent lumped-element-circuit models. The coupling element is represented as (i) a lumped capacitor in the case of direct capacitive coupling or (ii) an LC resonator in the case of MTL coupling. (c) Imaginary part of the transfer impedance Z_{21} of the capacitive and MTL coupling circuits for the set of parameters given in Table AI in Appendix C. Solid curves are the frequency dependence obtained from the distributed-circuit models, and dashed curves are from the equivalent-circuit models. The coupling strength between the resonators is $J/2\pi = 30$ MHz in both cases.

becomes (see Appendix B for details)

$$Z_{21}(\omega) = iZ_0 \frac{\sin\left(\frac{\omega\ell_c}{v}\right) \cos\left(\frac{\pi\omega}{2\omega_n}\right)}{\cos\left(\frac{\pi\omega}{2\omega_p}\right) \cos\left(\frac{\pi\omega}{2\omega_r}\right)} \left(\frac{c_m}{c}\right), \quad (1)$$

where $c = 1/(Z_0v)$ is the capacitance-to-ground per length of the CPW lines. The explicit dependence on the coupling inductance per length l_m has dropped out because in a homogeneous medium it is fully determined by the other line properties [31]. Here, it satisfies $l_m = Z_0^2 c_m$. The transfer impedance solution has its first zero at the frequency ω_n , which takes the form

$$\omega_n = \frac{\pi v}{2(\ell_r^s + \ell_c + \ell_p^s)}. \quad (2)$$

This frequency matches the anti-resonance of the effective $\lambda/2$ resonator with length $\ell_r^s + \ell_c + \ell_p^s$ that is formed between the shorted ends of the readout and filter resonators as depicted in Fig. 2(b). Due to its independence from the lengths ℓ_r^o and ℓ_p^o , the frequency ω_n can be tuned independently from the readout- and filter-resonator frequencies and can be designed at both positive and negative detunings from these modes. As a result, it is well suited for use as a notch filter to suppress the Purcell relaxation channel for a qubit in both positive and negative detuning regimes.

In order to simplify the analysis of the coupled resonators and to determine an expression for the coupling strength between them, we find an approximate mapping from the distributed-circuit representations in Fig. 3(a) to the lumped-element representations in Fig. 3(b). These lumped-element circuits accurately reproduce the electrical responses of the distributed circuits at frequencies around the $\lambda/4$ modes. The equations governing the mapping are provided in Appendix C. The $\lambda/4$ modes are converted to parallel LC resonators, the lumped-element capacitance C_J in Fig. 3(a)(i) is transformed to the capacitance \tilde{C}_J , and the MTL coupler in Fig. 3(a)(ii) is transformed to a parallel LC resonator with capacitance C_n and inductance L_n , satisfying $1/\sqrt{L_n C_n} = \omega_n$.

The $Z_{21}(\omega)$ values for the equivalent lumped-element circuits and the exact solution to the distributed circuits are compared in Fig. 3(c) for a given set of parameters, showing excellent correspondence at frequencies around the notch frequency ω_n and the $\lambda/4$ modes. We infer that the low-energy Hamiltonian for the distributed circuit closely matches the equivalent circuit Hamiltonian given the close correspondence of their electrical responses. The interaction Hamiltonian for the equivalent circuit with the MTL coupler depicted in Fig. 3(b)(ii) takes the form (see Appendix C for the derivation)

$$\hat{\mathcal{H}}_{\text{int}} = \hbar J (\hat{a}_r^\dagger \hat{a}_p + \hat{a}_r \hat{a}_p^\dagger), \quad (3)$$

$$J = \bar{\omega}_{rp} \frac{\pi^2}{32} \frac{\left(\frac{\bar{\omega}_{rp}}{\omega_n} - \frac{\omega_n}{\bar{\omega}_{rp}}\right)^3}{\cos^2\left(\frac{\pi\omega_n}{2\bar{\omega}_{rp}}\right)} \left(\frac{c_m}{c}\right) \sin\left(\frac{\omega_n \ell_c}{v}\right), \quad (4)$$

where $\bar{\omega}_{rp} = (\omega_r + \omega_p)/2$ is the average of the readout and filter-resonator frequencies, and we have taken $|\omega_r - \omega_p| \ll \omega_n$. The terms $\hat{a}_{r(p)}^\dagger$ and $\hat{a}_{r(p)}$ are the creation and annihilation operators for the readout- and filter-resonator modes, and we have used the rotating-wave approximation (RWA) to drop the non-photon-number-preserving terms. The exchange coupling J is suppressed as the notch frequency approaches $\bar{\omega}_{rp}$, scales linearly with the capacitance ratio c_m/c , and similarly scales linearly with the coupled-section length ℓ_c , given that $\omega_n \ell_c \ll v$. The capacitance ratio c_m/c can be determined efficiently using a conformal-mapping technique [34], which allows J to be predicted quickly for a given set of line dimensions. The dependence of c_m/c on the width d of the ground strip separating the coupled lines is plotted in Fig. 4(c). The notch frequency is to a good approximation independent of d , per Eq. (2). Thus, this width provides a parameter to tune the J coupling independently of the notch frequency.

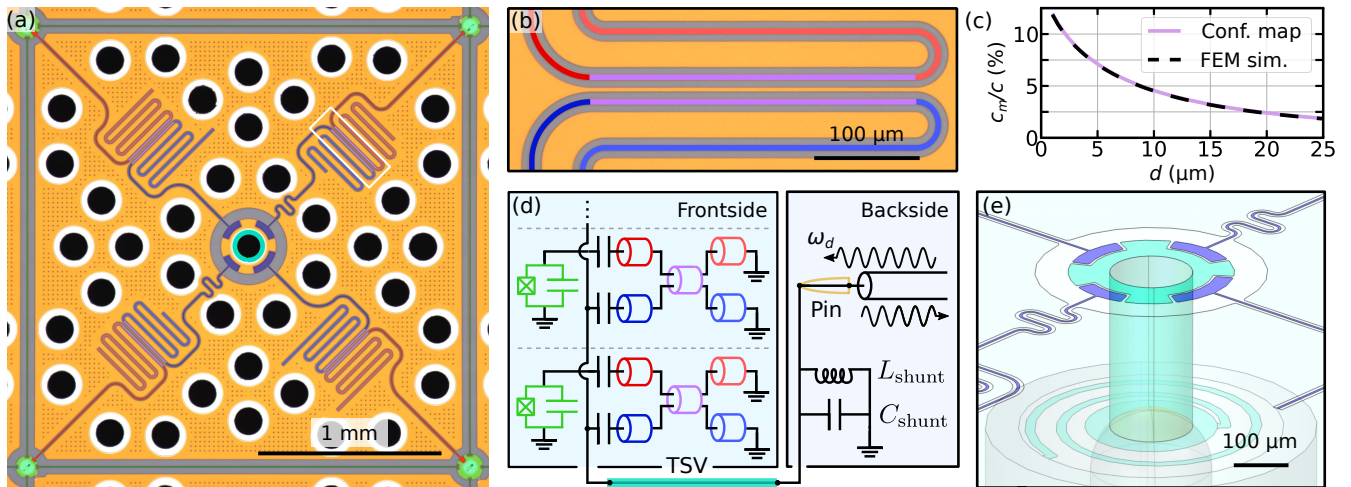


FIG. 4. (a) False-colored image of a four-qubit unit cell from a 16-qubit device. The four transmon qubits (green) are coupled to their nearest neighbors by capacitive buses (dark green). The four $\lambda/4$ readout resonators (red) couple to $\lambda/4$ dedicated filter resonators (blue), which couple to a shared readout line on the circuit backside through a TSV (teal). (b) Magnification of the region enclosed by the rectangle in (a), showing the MTL section (purple) that couples the readout resonator and filter resonator. The width of the ground strip separating the two center lines is $d = 3.8 \mu\text{m}$. (c) Ratio of the per-length capacitances c_m and c as a function of the ground strip width d , determined numerically using a conformal-mapping technique (solid) and from finite-element (FEM) simulation using COMSOL [35] (dashed). (d) Circuit diagram of the readout configuration for the unit cell. (e) Schematic three-dimensional transparent image of the TSV structure (teal) that routes signals from a pogo pin (yellow) on the circuit backside to the filter resonators on the circuit frontside. The TSV structure features a spiral inductor patterned on the circuit backside, which screens the parasitic shunt capacitance of the TSV structure.

C. Purcell-filtering enhancement

In order to quantify the effect of the notch on the Purcell filtering, we compare the predicted Purcell-limited energy relaxation times for a qubit that is coupled to the readout line through a readout resonator and filter resonator that are MTL coupled and capacitively coupled. The coupling strength J is assumed to be the same. We define the Purcell-filtering enhancement factor ξ as the ratio of these relaxation times. Employing the equivalent circuits from the previous section, the enhancement factor is given by (see Appendix D for the derivation)

$$\xi = \frac{1}{4} \frac{\omega_q^2}{\Delta_{qn}^2} \left(1 - \frac{\omega_n^2}{\omega_{rp}^2} \right)^2, \quad (5)$$

where ω_q and $\Delta_{qn} = \omega_q - \omega_n$ ($\Delta_{qn} \ll \omega_n$) are the qubit frequency and detuning from the notch, respectively. The enhancement diverges like $1/\Delta_{qn}^2$ as the qubit approaches the notch frequency. The expression can also be rearranged into a formula for the bandwidth B around the notch where the enhancement to the Purcell-limited relaxation time of the qubit is at least a factor of ξ ,

$$B \approx \frac{\omega_n}{\sqrt{\xi}} \left| 1 - \frac{\omega_n^2}{\omega_{rp}^2} \right|. \quad (6)$$

This expression predicts that, for the device parameters in the next section, the Purcell filtering is enhanced by at least two orders of magnitude over bandwidths exceeding 200 MHz around the notch frequency.

III. EXPERIMENTAL RESULTS

A. Purcell protection of the qubit relaxation

We fabricated a 16-qubit device with each qubit coupled to a readout resonator and dedicated filter resonator featuring MTL coupling and notch frequencies that were tuned to the respective target qubit frequencies. The device architecture is based on a four-qubit unit cell that is tiled to create an array of fixed-frequency transmon qubits with nearest-neighbor couplings. Figure 4(a) shows one of the four-qubit unit cells, featuring TiN-based transmon qubits and resonators, and superconducting through-silicon vias (TSVs) metalized with Al. The TSVs connect the frontside ground planes via a common backside ground plane, and as a result airbridges [36] are not used. Readout is performed by a reflection measurement through a pogo pin which contacts a TSV on the backside of the chip. Signals are routed to the filter resonators through the TSV as depicted in Fig. 4(d). Figure 4(e) shows a scale diagram of the through-substrate readout design. The TSV structure has a large (~ 230 fF) parasitic shunt capacitance to ground, which reduces the external linewidth of the filter resonators. In order to mitigate this, a spiral shunt inductor is patterned on the circuit backside to screen the shunt capacitance around the readout frequencies (see Appendix E for details).

Figure 5(a) shows the reflected phase response of a signal applied to the readout pogo pin on the circuit backside. Due to the relatively small detuning between the

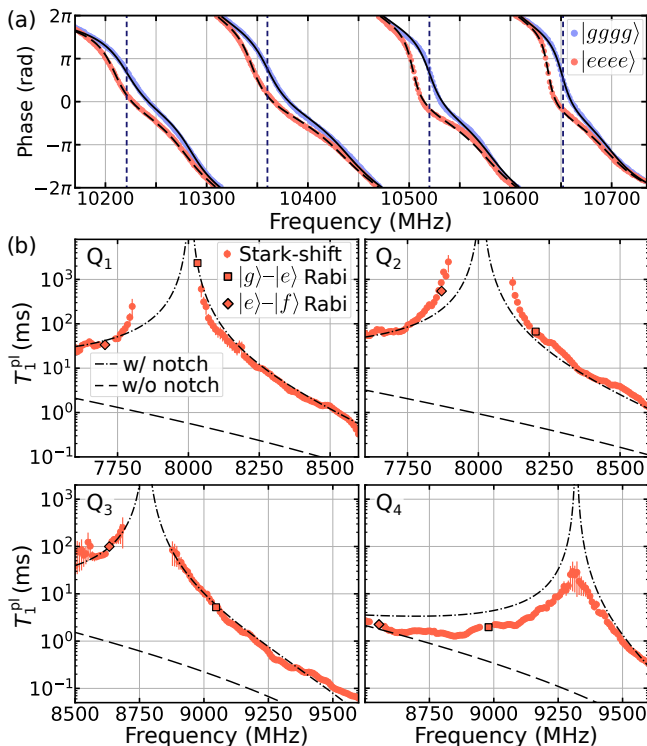


FIG. 5. (a) Reflection spectra of the four readout-resonator and filter-resonator pairs for the four qubits prepared in the $|g\rangle$ (blue) and $|e\rangle$ (red) states. The phase is wrapped modulo 4π to better visualize the response of each readout- and filter-resonator pair. The solid and dashed lines show the fitted phase response for the $|g\rangle$ - and $|e\rangle$ -state preparations, respectively. The vertical dashed lines show the four readout mode frequencies $\omega_{r_o}^g$. (b) Purcell-limited relaxation time T_1^{pl} of the four qubits as a function of frequency inferred from the Rabi oscillations driven at the qubit $|g\rangle$ - $|e\rangle$ and $|e\rangle$ - $|f\rangle$ transition frequencies (squares and diamonds, respectively) and the ac Stark shift induced by the drive detuned from these transitions (dots). The dot-dashed and dashed black lines show the prediction of a circuit model with and without the intrinsic notch filtering, respectively.

filter resonators compared to their external linewidths, the parameters of the four readout resonators and four filter resonators were fitted simultaneously to a reflection model that encompassed all eight resonators in the four-qubit unit cell (see Appendix E for details). By fitting the $|g\rangle$ - and $|e\rangle$ -state responses simultaneously, the dispersive shifts of the readout resonators were also determined. The readout-mode parameters determined from the fit, together with the qubit parameters for qubits Q_1 to Q_4 determined from their spectroscopy, are presented in Table I. Here, the readout modes refer to the hybridized modes formed between the readout and filter resonators which were addressed during the qubit readout (see Appendix E for details). The bare readout- and filter-resonator parameters are also presented in Table AII in Appendix E.

The Purcell protection of each qubit was characterized

TABLE I. Qubit and readout parameters. Here, ω_q and α are the qubit frequency and anharmonicity, respectively. The terms $\omega_{r_o}^g$ and $\omega_{r_o}^e$ are the hybridized readout mode frequencies given the qubit is in the $|g\rangle$ and $|e\rangle$ state, respectively, and χ_{r_o} is the readout mode dispersive shift defined $\omega_{r_o}^e \equiv \omega_{r_o}^g + 2\chi_{r_o}$. The term T_1^{pl} is the Purcell-limited relaxation time evaluated at the qubit frequency and ξ is the predicted Purcell-filtering enhancement factor due to the intrinsic notch filter.

	$\omega_q/2\pi$ (MHz)	$\alpha/2\pi$ (MHz)	$\omega_{r_o}^g/2\pi$ (MHz)	$\kappa_{r_o}^g/2\pi$ (MHz)	$\chi_{r_o}/2\pi$ (MHz)	T_1^{pl} (ms)	ξ
Q_1	8032	-326	10221	42	-5.9	2300	~ 3000
Q_2	8189	-333	10360	34	-7.8	70	85
Q_3	9046	-414	10520	24	-8.3	5	25
Q_4	8980	-425	10652	19	-7.1	2	10

following the method in Ref. 16. First, the drive power P incident on the device was calibrated by measuring the ac Stark shift of the qubit caused by a readout tone (see Appendix F for details). The drive amplitude Ω incident on the qubit was then determined by two methods: (i) by measuring the induced Rabi-oscillation frequency in the qubit when the drive was on-resonance with the $|g\rangle$ - $|e\rangle$ and $|e\rangle$ - $|f\rangle$ transitions and (ii) by measuring the drive-induced Stark shift on the qubit when the drive was detuned from these transitions. The Purcell-limited relaxation time T_1^{pl} over a range of frequencies was then determined from the ratio of P and Ω^2 (see Appendix F for details). The Purcell-limited relaxation times for the four qubits are shown in Fig. 5(b). The predicted values using an equivalent-circuit model of the readout with and without the intrinsic notch filtering are overlaid (see Appendix D for details). The notch frequency is the only fitting parameter in these models, with the circuit otherwise determined from the qubit and readout parameters. The Purcell-limited relaxation times at the $|g\rangle$ - $|e\rangle$ transition frequency, and the predicted relaxation enhancement factors ξ are presented in Table I. The evaluated Purcell-limited relaxation times all exceed 2 ms and are predicted to be enhanced by at least an order of magnitude due to the intrinsic notch filtering. In the case of qubit Q_1 , the notch frequency is nearly resonant with the qubit frequency, and as a result the measured value of T_1^{pl} approaches 2.5 s even though the effective readout linewidth is 42 MHz, demonstrating the effective elimination of the Purcell relaxation channel.

Figure 6 compares the measured notch frequencies and coupling strengths J to the predictions of Eqs. (2) and (4), respectively. The phase velocity v and the capacitance ratio c_m/c in the symbolic expressions were determined numerically by conformal mapping. The measured values of the notch frequencies ω_n were used in Eq. (4) to calculate the J values, in order to assess the accuracy of the two expressions independently. The measured notch frequencies and J couplings on average differ from the predicted values by 5% and 19%, respectively. The underestimation of the coupling strengths is in part

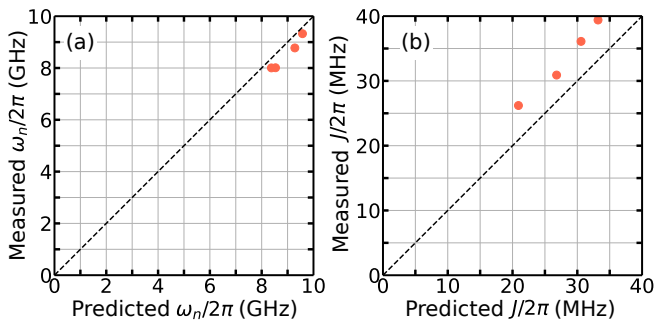


FIG. 6. Evaluation of the symbolic solutions for (a) the predicted notch frequency ω_n and (b) the coupling strength J . The measured values are compared to the predictions of Eqs. (2) and (4) for the four readout- and filter-resonator pairs.

due to the assumption that coupling only occurs along the MTL-section-length ℓ_c as defined in Fig. 4(b), since this neglects the coupling between the curved sections of the lines.

B. Multiplexed fast readout

Figure 7(a) shows the time dependence of the separation $S(t) \equiv |s_{\text{out}}^e(t) - s_{\text{out}}^g(t)|$ of the qubit-state-dependent coherent output fields $s_{\text{out}}^{g(e)}$ from the device in response to a 100-ns-long rectangular tone applied at the optimal readout frequency of qubit Q_2 . The measured state-dependent heterodyne signals were converted to the separation through the relationship $\Gamma_m = S_{\text{ss}}^2/2$ between the measurement-induced dephasing rate Γ_m and the steady-state separation S_{ss} [37]. The measurement displays a short transient period of around 50 ns before the output field carries the maximum information about the qubit state. A semi-classical model for the output-field separation (see Appendix E) evaluated using the independently determined readout- and filter-resonator parameters shows good correspondence to the measured dynamics.

The rapid rise in output-field separation enabled the tune-up of a 56-ns multiplexed readout on the four qubits with high fidelity. For single-shot readout, a flux-driven impedance-matched parametric amplifier [38] was used in the phase-preserving mode of operation. At the optimal point, the quantum efficiency η of the readout chain was determined to be {27, 46, 40, 42}% for qubits Q_1 to Q_4 , respectively, by comparing the measurement-induced dephasing to the measured signal-to-noise ratio (SNR) [39].

Figures 7(b) and 7(c) show the pulse sequences used to benchmark the readout assignment fidelity F and the quantum non-demolition (QND) fidelity F_Q , respectively. The pulse sequences were carried out on the four qubits simultaneously and repeated 4×10^4 times both with and without the π -pulse. The two-step measurement pulses featured an initial 14-ns flat top with a 6-

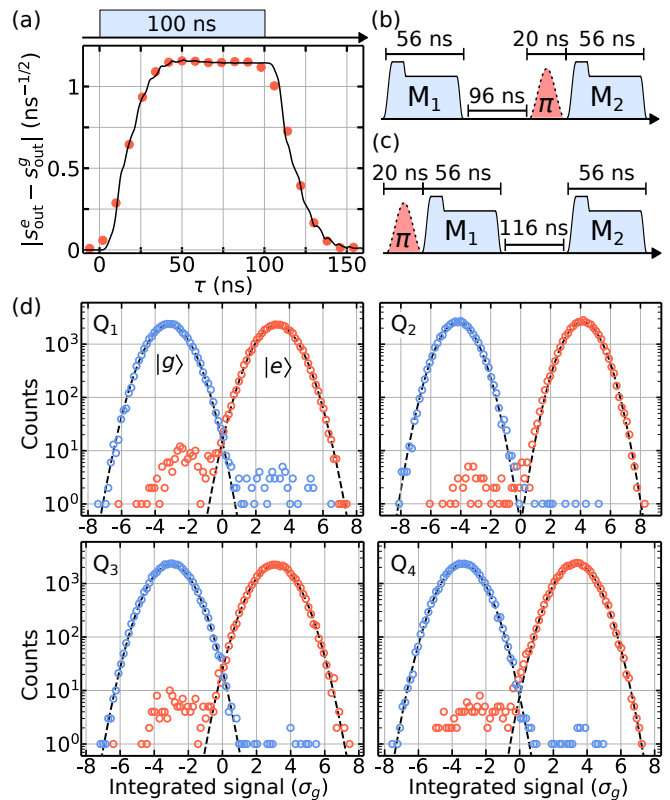


FIG. 7. Demonstration of fast readout. (a) Time dependence of the output-field separation $S(t) \equiv |s_{\text{out}}^e(t) - s_{\text{out}}^g(t)|$ in response to a 100-ns-long rectangular readout pulse at the optimal readout frequency of qubit Q_2 , averaged over 4×10^4 repetitions. The solid black line is the prediction of the semi-classical model for the coherent output fields. (b) and (c) Readout pulse sequences used to determine the assignment and QND fidelities, respectively. The readout sequences are performed with and without the 20-ns-long π -pulse. (d) Histograms of simultaneous time-integrated single-shot signals for the four qubits projected along the principal axes in the in-phase and quadrature (IQ) plane. Dashed lines show the fits of the $|g\rangle$ - and $|e\rangle$ -state signal distributions to Gaussian distributions. The horizontal axes are normalized by the standard deviation σ_g of the $|g\rangle$ -state Gaussian distribution.

ns raised-cosine edge and a flat-top amplitude between 1.35–1.4 times higher than that of the subsequent flat plateau in order to increase the output-field separation at early times. The steady-state photon-number populations of the readout resonators during the main pulse step, $n_{r,j}^g$ (given the qubit is in the $|g\rangle$ state), are provided in Table II as a fraction of the critical photon number [40]. The acquired measurement signals were averaged over an optimally-weighted integration time window of 56 ns. The qubit states were assigned from the integrated signals using a two-state logistic-regression discrimination model [41] that was trained on a prior dataset of 2×10^4 single-shot measurements. The assignment fidelities were determined using the definition $F \equiv [P_0(g_2|g_1) + P_\pi(e_2|g_1)]/2$, where $P(a|b)$ denotes

the probability of event a given event b . The subscripts 1 and 2 refer to the first and second measurement outcomes, and the subscripts π and 0 refer to the pulse sequences in Fig. 7(b) with and without the π -pulse. The QND fidelities were determined from the QND pulse sequences in Fig. 7(c) using the definition $F_Q \equiv [P_0(g_2|g_1) + P_\pi(e_2|e_1)]/2$. The resulting assignment and QND errors are summarized in Table II along with the predicted coherence-limited error imposed by qubit relaxation.

Figure 7(d) shows the histograms formed by projecting the single-shot IQ points from the second measurement of the assignment fidelity pulse sequence along the principal axis. The results are post-selected to ensure the qubit was in the $|g\rangle$ state prior to the π -pulse. The histogrammed signals closely match Gaussian distributions with outliers that are discussed below. From the overlap of the Gaussian fits the state-separation errors ε_{sep} are calculated and summarized in Table II.

The average assignment fidelity for the 56-ns simultaneous measurement is 99.77%, representing a significant advancement for fast multiplexed qubit readout [15]. Focusing on qubit Q₂, the separation error was negligible and the assignment fidelity of 99.91(1)% reached the coherence limit. The probability of measurement-induced excitation from $|g\rangle$ to $|e\rangle$ was low with $P_0(e_2|g_1) = 0.03\%$. In Appendix G, the IQ plot is examined, showing that less than 0.01% of measurements exhibited discernible excitation to leakage states [42–44]. The QND fidelity was 0.37% below the coherence limit, implying some activation of measurement-induced leakage and measurement-induced relaxation [45, 46]. On the other hand, the assignment and QND fidelities for qubit Q₁ (which had the lowest quantum efficiency) and Q₃ were markedly lower than their respective coherence limits, implying that the readout pulse caused significant measurement-induced excitation and relaxation. The IQ plot for Q₁ reveals measurement-induced excitation to leakage states that contributed significantly to the assignment error (see Appendix G). This could be countered with improved parametric amplification at the readout frequency of Q₁, which would facilitate readout at a reduced photon number. Pseudo-syndrome detection benchmarking could be performed to build a more complete picture of the measurement-induced leakage [28]. Additional optimizations could be achieved by more advanced readout pulse shaping [47, 48]. Further increasing the assignment fidelities beyond 99.9% will require increasing the qubit relaxation times. The averaged qubit relaxation times T_1 of qubit Q₁ to Q₄ in the current experiments were {45(6), 26(1), 38(1), 34(1)} μs at the time of the readout benchmarking.

The results demonstrate that tailoring readout modes to have large external linewidths and dispersive shifts is an effective strategy to increase assignment fidelities, in agreement with Refs. 14 and 17. A potential drawback of this approach is that it increases the susceptibility of qubits to dephasing due to the noise-photon

TABLE II. Readout results. Here, $n_{r,j}^g/n_{\text{crit}}$ represents the ratio of the steady-state photon number in the readout resonator during the readout pulse to the critical photon number. The terms ε and ε_Q are the assignment and QND errors, respectively, defined $\varepsilon \equiv 1 - F$ and $\varepsilon_Q \equiv 1 - F_Q$. The terms ε_{cl} and $\varepsilon_{\text{cl}}^Q$ are the coherence-limited error budgets on the assignment and QND fidelity, estimated from measurements of the qubit relaxation time carried out within an hour of the readout benchmarking. Details of the coherence limits and separation error calculations are given in Appendix G

	$n_{r,j}^g/n_{\text{crit}}$	ε (%)	ε_{cl} (%)	ε_Q (%)	$\varepsilon_{\text{cl}}^Q$ (%)	ε_{sep} (%)
Q ₁	1.50	0.35(2)	0.06	1.91(5)	0.19	0.08
Q ₂	1.05	0.09(1)	0.11	0.70(3)	0.33	<0.01
Q ₃	0.82	0.29(2)	0.07	1.10(4)	0.23	0.13
Q ₄	0.89	0.20(2)	0.08	0.55(3)	0.25	0.04

population in the readout resonator [49–51]. However, we expect some degree of protection from this dephasing channel in this device due to the high readout resonator frequencies, which were all above 10 GHz. This is because a thermal photon population in the readout resonator is expected to follow Bose-Einstein statistics [52] and thus be exponentially suppressed with increasing frequency at a given temperature. The Hahn-echoed pure dephasing times $T_{2\text{echo}}$ of qubits Q₁ to Q₄ were found to be {61, 55, 152, 77} μs . Attributing this dephasing entirely to the noise-photon population $n_{r,j}^{\text{noise}}$ of the readout resonators sets upper bounds of $n_{r,j}^{\text{noise}} \leq \{3.1, 3.2, 1.0, 2.4\} \times 10^{-4}$ (see Appendix E for details). These values correspond to effective temperatures of between 55 to 62 mK as a result of the high readout resonator frequencies. It may be possible to further suppress the sensitivity to noise-photon induced dephasing by introducing weak anharmonicity to the filter resonators [18].

IV. CONCLUSION

We have shown that by coupling a quarter-wavelength readout resonator and filter resonator together, both capacitively and inductively, it is possible to engineer an intrinsic notch filter that can provide strong auxiliary Purcell filtering to the qubit. An equivalent-circuit model has been introduced and used to find symbolic expressions for the notch filtering and for the coupling strength between the readout and filter resonators. We have experimentally verified these formulas in a device with four-to-one readout multiplexing. The notch filter broadens the range of linewidths for the readout mode that are possible without impacting the qubit relaxation time. By designing readout modes with external linewidths as large as 42 MHz, we tuned up a fast (56-ns) multiplexed readout across four qubits and benchmarked a state-of-the-art average simultaneous assignment fidelity of 99.77%, with the highest qubit assignment fidelity equal to 99.91%.

The compact coupled resonators with intrinsic notch filtering offer strong Purcell protection and are straightforward to design, making this an attractive circuit component for superconducting qubit readout.

ACKNOWLEDGMENTS

The work was supported in part by the Ministry of Education, Culture, Sports, Science and Technology (MEXT) Quantum Leap Flagship Program (Q-LEAP) (Grant No. JPMXS0118068682), and the JSPS Grant-in-Aid for Scientific Research (KAKENHI) (Grant No. JP22H04937).

Appendix A: Device and experimental setup

The four-qubit unit cell measured in this work is from the 16-qubit device shown in Fig. A1(a). The qubits are coupled to nearest neighbors (NN) by short transmission-line sections, resulting in an effective capacitive coupling between nearest neighbors. The average NN coupling strength is 7.0 MHz, and the NN static-ZZ crosstalk ranges between 80 to 200 kHz. The circuit backside where the qubit- and readout-drive wirings make contact with the chip is shown in Fig. A1(b). Figure A1(c) shows a close up of the TSV contacted by a readout pogo pin which routes readout signals to the circuit frontside.

The device was cooled to ~ 20 mK inside a Bluefors XLD1000 dilution refrigerator. The experimental setup is shown in Fig. A2. For the qubit and readout drives, the impedance-matched parametric amplifier pump drive, and the readout signal acquisition, a QuEL-1 controller (QuEL Inc. [53]) was used. For the experiments characterizing the Purcell filtering, the readout drive was combined with a qubit drive which was used to generate the Stark shifting tone. In this configuration, a room-temperature amplifier (Mini-circuits ZVA-183W-S+) was attached to the Stark-shifting qubit drive in order to increase the Stark shift induced in the qubit.

Appendix B: Transfer impedance between two MTL-coupled $\lambda/4$ resonators

In this section, we derive an analytic solution for the transfer impedance between two MTL-coupled $\lambda/4$ resonators. We outline the necessary assumptions for achieving a tractable solution and demonstrate that these assumptions are well justified for the coupled CPW lines in this work. We discuss the general solution as well as the specific cases of lumped-element capacitive coupling and MTL coupling in a homogeneous medium.

Figure A3(a) shows an image of two coupled CPW lines of the kind used in this work to couple the readout and filter resonators. The key line dimensions are the ground

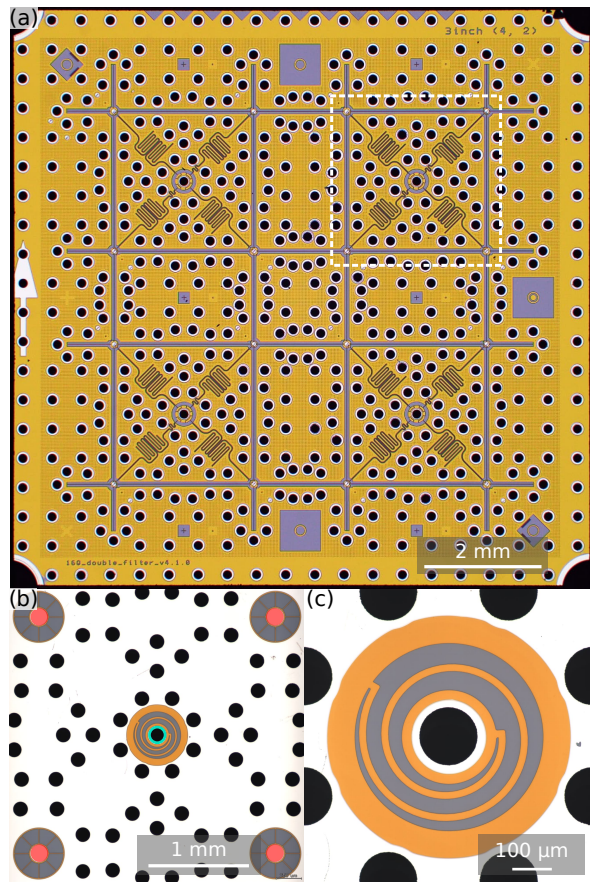


FIG. A1. Images of the 16-qubit device. (a) Photograph of the 16-qubit chip. The four-qubit unit cell measured in this work is highlighted. (b) False-color image of the backside of the four-qubit unit cell, showing the contact pads where pogo pins contact the chip for qubit control (red) and for multiplexed qubit readout (teal). (c) Image of the TSV contacted by the readout pogo pin, showing the TiN spiral shunt inductor.

separation $s = 7.5 \mu\text{m}$, the center-line width $w = 5 \mu\text{m}$, and the width of the ground strip that separates the two CPWs, d , which took values between $3.8 \mu\text{m}$ and $5.5 \mu\text{m}$.

The two coupled CPW lines are treated as an MTL with per-length parameters as defined in Fig. A3(b). In order to find a tractable symbolic solution for the transfer impedance $Z_{21}(\omega)$ between two $\lambda/4$ resonators coupled together by this MTL, the following assumptions are applied:

- Cyclic-symmetric lines: The two lines of the MTL are both taken to have the same capacitance-to-ground and self-inductance per length, here denoted c_c and l_c , respectively.
- Weakly-coupled lines: An excitation applied to one line of the MTL will induce an excitation in the other line. The weak-coupling assumption amounts to neglecting the back-action of this induced excitation onto the first line and is valid

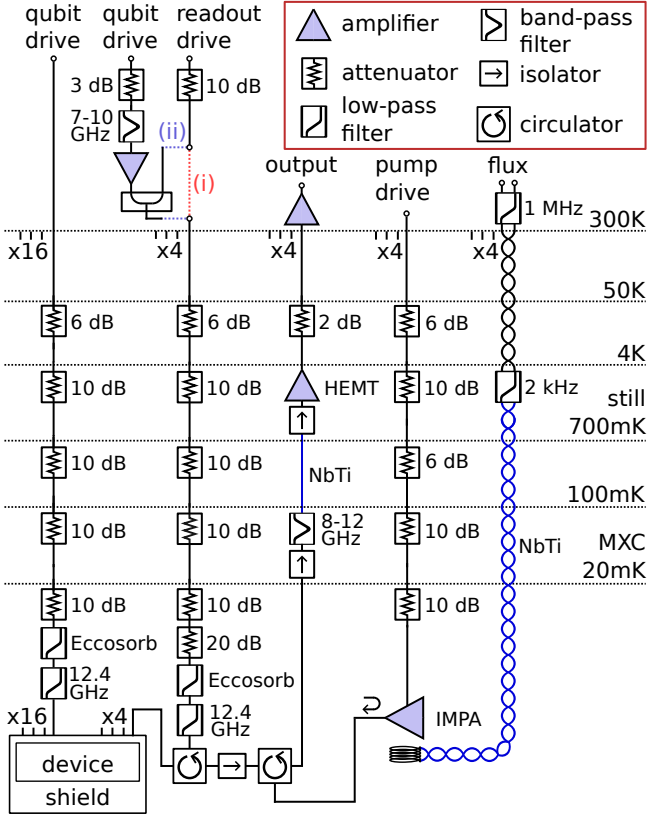


FIG. A2. Experimental setup. The readout drive line was wired in two configurations. In configuration (i), the readout drive is connected directly to the input line. In configuration (ii), it is combined with an amplified qubit drive before connecting to the input line. The IMPA amplifier refers to the impedance-matched parametric amplifier. The term MXC refers to the mixing chamber stage.

when $l_m \ll l_c$ and $c_m \ll c_c$. In a homogeneous medium, this is relaxed to the less restrictive condition $k \equiv (1 - (l_m/l_c)^2)^{1/2} \approx 1$ [54].

- Consonant lines: The two lines of the MTL have characteristic impedance and phase velocity defined as $Z_c \equiv \sqrt{l_c/(c_c + c_m)}$ and $v_c \equiv 1/\sqrt{l_c(c_c + c_m)}$, respectively. Here, the term consonant line is defined to mean that these quantities equal the characteristic impedance and phase velocity for the uncoupled sections of the $\lambda/4$ resonators, such that $Z_c = Z_0$ and $v_c = v$.

Figure A3(c) presents COMSOL finite-element simulation results showing that the weak-coupling and consonant-line assumptions are well justified for the coupled CPW lines considered in this work. The simulation results also confirm the relationship $Z_m = Z_c$ for two coupled CPW lines, where $Z_m \equiv \sqrt{l_m/c_m}$. As discussed later in Appendix B2, this relationship is characteristic of lines that are embedded in a homogeneous medium.

Figure A4(a) shows the distributed circuit used to model the coupled resonators, with a current source at-

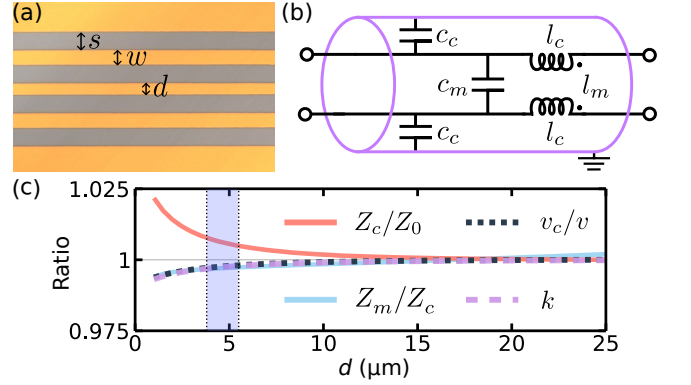


FIG. A3. Analysis of coupled CPW lines. (a) Image of the coupled CPW lines used to realize the MTL section. (b) Definitions for the per-length parameters of the two-line MTL. (c) Finite-element electrostatic simulation results using COMSOL for the coupled CPW lines showing dimensionless quantities of the MTL lines as a function of the width d of the separating ground strip. The values of d for the coupled CPW lines in this work lie inside the blue highlighted region.

tached to port 1. The transfer impedance between ports 1 and 2 is defined as $Z_{21}(\omega) \equiv V_2(\omega)/I_1(\omega)|_{I_2=0}$. In order to solve for this, the problem is broken down into parts as depicted in Figs. A4(b)–(d). First, the ratio $V_A(\omega)/I_1(\omega)$ is solved for, where $V_A(\omega)$ is the voltage at port A of the MTL. Using the weak-coupling assumption to neglect back-action and using the consonant-line assumption to set $Z_c = Z_0$ and $v_c = v$, the problem reduces to that of solving for the voltage at a distance ℓ_r^o from the open end of a shorted transmission line of total length $\ell_r = \ell_r^o + \ell_c + \ell_r^s$, as depicted in Fig. A4(b). This yields

$$\frac{V_A(\omega)}{I_1(\omega)} = iZ_0 \left[\tan\left(\frac{\omega\ell_r}{v}\right) \cos\left(\frac{\omega\ell_r^o}{v}\right) - \sin\left(\frac{\omega\ell_r^o}{v}\right) \right]. \quad (\text{B1})$$

Next, the voltage $V_C(\omega)$ at port C of the MTL line is solved for in terms of the voltage $V_A(\omega)$, as depicted in Fig. A4(c). Here, we make use of the general solution presented in Eq. (26a) of Ref. 54 for a weakly-coupled two-line MTL terminated with arbitrary loads. We use the consonant-line assumption to set $Z_c = Z_0$ and $v_c = v$ and after some algebraic manipulations arrive at the following expression,

$$\frac{V_C(\omega)}{V_A(\omega)} = Z_0\omega\ell_c c_m \frac{(A_+ - A_-) \cos\left(\frac{\omega\ell_p^o}{v}\right)}{2 \cos\left(\frac{\pi\omega}{2\omega_p}\right) \sin\left[\frac{\omega(\ell_r^s + \ell_c)}{v}\right]}, \quad (\text{B2})$$

where

$$A_+ = \left(1 + Z_m^2/Z_0^2\right) \text{sinc}\left(\frac{\omega\ell_c}{v}\right) \cos\left[\frac{\omega(\ell_r^s + \ell_p^s + \ell_c)}{v}\right], \quad (\text{B3})$$

$$A_- = \left(1 - Z_m^2/Z_0^2\right) \cos\left[\frac{\omega(\ell_r^s - \ell_p^s)}{v}\right]. \quad (\text{B4})$$

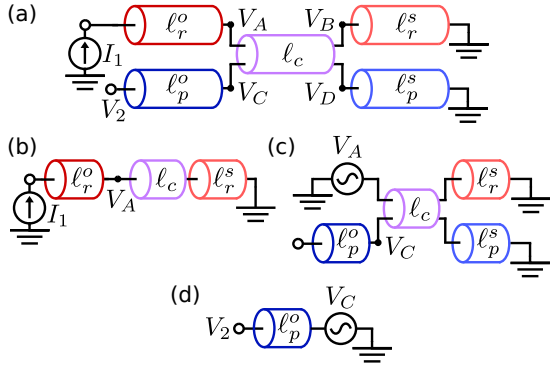


FIG. A4. Solution steps for determining the transfer impedance $Z_{21}(\omega)$. (a) Distributed-circuit model for two MTL-coupled $\lambda/4$ resonators. A current source drives port 1, and the goal is to determine the induced voltage V_2 at port 2. The induced voltages at the four ports of the MTL are defined as V_A to V_D . (b) Circuit used to find the voltage V_A in terms of the current drive I_1 . (c) Circuit used to find the voltage V_C in terms of the voltage drive V_A . (d) Circuit used to find the voltage V_2 in terms of the voltage drive V_C .

Here, we restate that $Z_m \equiv \sqrt{l_m/c_m}$. Finally, the voltage V_2 is solved for in terms of the voltage V_C as depicted in Fig. A4(d), yielding

$$\frac{V_2(\omega)}{V_C(\omega)} = \sec\left(\frac{\omega \ell_p^o}{v}\right). \quad (\text{B5})$$

The transfer impedance is found by combining these solutions:

$$Z_{21}(\omega) = \left(\frac{V_2}{V_C}\right) \left(\frac{V_C}{V_A}\right) \left(\frac{V_A}{I_1}\right). \quad (\text{B6})$$

Substituting in Eqs. (B1), (B2) and (B5), the overall expression simplifies to yield the final result

$$Z_{21}(\omega) = iZ_0^2 \omega \ell_c c_m \frac{A_+ - A_-}{2 \cos\left(\frac{\pi\omega}{2\omega_r}\right) \cos\left(\frac{\pi\omega}{2\omega_p}\right)}. \quad (\text{B7})$$

This solution has the required properties of being purely imaginary and reciprocal such that $Z_{12}(\omega) = Z_{21}(\omega)$. This approach can also be applied to find tractable solutions in the case where one of the resonators is mirrored through a line bisecting the MTL section, as well as in the cases where one or both of the resonators are replaced with $\lambda/2$ resonators. Furthermore, under the weak-coupling and consonant-line assumptions, the solution generalizes to resonators that are connected by multiple MTL sections. In this case, the transfer impedance is found by summing the contributions coming from each MTL section treated independently, as depicted in Fig. A5. In this way, Eq. (B7) can also be used for modeling the response and predicting notch frequencies for resonators that are coupled by multiple MTL sections.

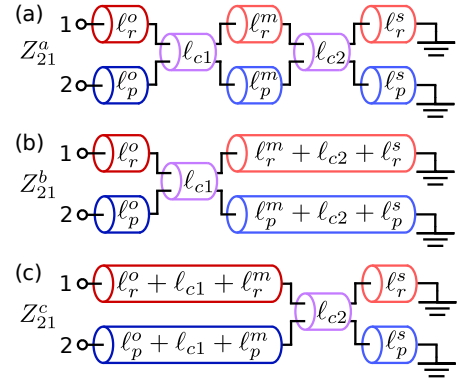


FIG. A5. (a) Pair of $\lambda/4$ resonators coupled by two MTL sections. The transfer impedance is defined Z_{21}^a . (b) and (c) Same pair of resonators coupled by only the first and second MTL sections, respectively. Under the weak-coupling and consonant-line assumptions, the transfer impedances satisfy the relation $Z_{21}^a = Z_{21}^b + Z_{21}^c$.

1. Capacitive coupling

As stated in the main text, lumped-element capacitive coupling represents a special case of the MTL coupling found by taking the limits $c_m \ell_c \rightarrow C_J$ and $l_m, \ell_c \rightarrow 0$. In this case, the solution for $Z_{21}(\omega)$ given in Eq. (B7) reduces to

$$Z_{21}(\omega) = -iZ_0^2 \frac{\sin\left(\frac{\omega \ell_r^s}{v}\right) \sin\left(\frac{\omega \ell_p^s}{v}\right)}{\cos\left(\frac{\pi\omega}{2\omega_r}\right) \cos\left(\frac{\pi\omega}{2\omega_p}\right)} \omega C_J. \quad (\text{B8})$$

This expression has its first zeros at frequencies $\pi v/\ell_r^s$ and $\pi v/\ell_p^s$. These terms satisfy $\pi v/\ell_r^s \geq 2\omega_r$ and $\pi v/\ell_p^s \geq 2\omega_p$, leading to the bound on the notch frequency $\omega_n \geq \min(2\omega_r, 2\omega_p)$ that is stated in the main text.

2. MTL coupling

For a two-line, cyclic-symmetric MTL in a homogeneous medium with relative permittivity ϵ_r , the per-length capacitances and inductances are constrained to obey to relations [31]

$$l_c(c_c + c_m) - l_m c_m = \mu_0 \epsilon_0 \epsilon_r, \quad (\text{B9})$$

$$Z_m = Z_c. \quad (\text{B10})$$

Substituting Eq. (B10) into Eq. (B7) and using the consonant-line assumption to set $Z_c = Z_0$, the solution for $Z_{21}(\omega)$ reduces to

$$Z_{21}(\omega) = iZ_0 \frac{\sin\left(\frac{\omega \ell_c}{v}\right) \cos\left(\frac{\pi\omega}{2\omega_n}\right)}{\cos\left(\frac{\pi\omega}{2\omega_r}\right) \cos\left(\frac{\pi\omega}{2\omega_p}\right)} \left(\frac{c_m}{c}\right). \quad (\text{B11})$$

Here, ω_n is the notch frequency where $Z_{21}(\omega) = 0$, which we restate takes the form

$$\omega_n = \frac{\pi v}{2(\ell_r^s + \ell_c + \ell_p^s)}. \quad (\text{B12})$$

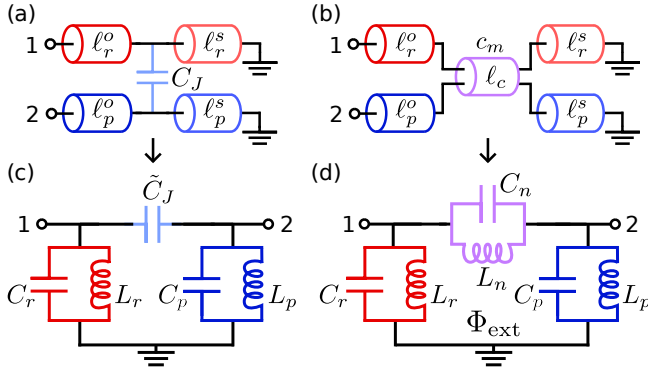


FIG. A6. Distributed circuits and corresponding equivalent lumped-element circuits for the coupled readout and filter resonators. The equivalent-circuit models are used to determine the coupling strength between the $\lambda/4$ modes of the readout resonator and filter resonator, for the cases of (a)[(c)] lumped-element capacitive coupling, and (b)[(d)] MTL coupling.

Appendix C: Equivalent lumped-element circuits and interaction Hamiltonians

In this section, we provide a mapping between the distributed and equivalent lumped-element circuits shown in Fig. A6. The mapping is chosen such that the equivalent circuits closely match the electrical response of the distributed circuits around the readout- and filter-resonator frequencies. The calculated transfer impedances for the distributed and equivalent circuits are shown in Fig. 3(c) of the main text for the particular set of circuit parameters given in Table AI, indicating good agreement. Given the electrical responses closely match, we infer that the interaction Hamiltonians for both the distributed and equivalent circuits are also closely matched.

We first review that a $\lambda/4$ transmission-line resonator with length ℓ has its fundamental resonance at $\omega_{\lambda/4} = \pi v/(2\ell)$ and that at frequencies near this resonance the electrical response is well approximated by a parallel LC resonator with lumped-element values given by [55]

$$C_{\lambda/4} = \frac{c\ell}{2}, \quad L_{\lambda/4} = \frac{8\ell}{\pi^2}, \quad (\text{C1})$$

where c and l are the capacitance and inductance per length of the line, respectively, satisfying $c = 1/(Z_0 v)$ and $l = Z_0/v$. Using this result, the lumped-element capacitance and inductance of the readout resonator and filter resonator are mapped from the distributed circuit by the relations,

$$C_{r(p)} = \frac{\ell_{r(p)}}{2Z_0 v}, \quad L_{r(p)} = \frac{8Z_0 \ell_{r(p)}}{\pi^2 v}. \quad (\text{C2})$$

The characteristic impedances of the lumped-element resonators, defined $Z_{r(p)} \equiv \sqrt{L_{r(p)}/C_{r(p)}}$, are related to the transmission-line characteristic impedance by the formula

$$Z_{r(p)} = \frac{4Z_0}{\pi}. \quad (\text{C3})$$

TABLE AI. Readout- and filter-resonator dimensions used to calculate the transfer impedances plotted in Fig. 3(c) of the main text. The Cap(MTL) parameters were used to calculate the transfer impedance for the distributed circuit with the lumped-element coupling capacitor(MTL coupler). The value of C_J was set to 1.4 fF, and the value of c_m was set to 8.5 fF/mm in order to match the coupling strengths. Values of $v = 1.19 \times 10^8$ m/s and $Z_0 = 66 \Omega$ were used for the phase velocity and characteristic impedance of the lines. The MTL parameters match the designed parameters for the readout and filter resonators of Q_1 .

	ℓ_r^o (μm)	ℓ_r^s (μm)	ℓ_p^o (μm)	ℓ_p^s (μm)	ℓ_c (μm)	d (μm)
Cap	1133	1776	918	1818	–	–
MTL	974	1617	759	1659	318	5.5

1. Capacitive coupling

Figure A6(c) depicts the equivalent circuit for the capacitively coupled $\lambda/4$ resonators. Equating the transfer impedance $Z_{21}^{ec}(\omega)$ for the equivalent circuit with the transfer impedance for the distributed circuit in Fig. A6(a) [given by Eq. (B8)] yields the following expression for the ratio between the equivalent-circuit capacitance \tilde{C}_J and the distributed-circuit capacitance C_J ,

$$\frac{\tilde{C}_J}{C_J} = \frac{\pi^2}{16} \frac{\left(\frac{\omega_r}{\omega} - \frac{\omega}{\omega_r}\right) \left(\frac{\omega_p}{\omega} - \frac{\omega}{\omega_p}\right)}{\cos\left(\frac{\omega\pi}{2\omega_r}\right) \cos\left(\frac{\omega\pi}{2\omega_p}\right)} \sin\left(\frac{\ell_r^s \omega}{v}\right) \sin\left(\frac{\ell_p^s \omega}{v}\right), \quad (\text{C4})$$

where the weak-coupling assumption $\tilde{C}_J \ll C_r, C_p$ has been used. This ratio is frequency-dependent. However the frequency dependence is weak around the $\lambda/4$ -mode frequencies ω_r and ω_p . In order to determine a frequency-independent value for \tilde{C}_J that is accurate around these modes, the expression is separated into readout-resonator- and filter-resonator-dependent factors, and these are then evaluated with ω set to the corresponding resonance frequencies

$$\frac{\tilde{C}_J}{C_J} \approx \left(\frac{\pi}{4}\right)^2 A_r A_p, \quad (\text{C5})$$

$$A_r = \left[\frac{\left(\frac{\omega_r}{\omega} - \frac{\omega}{\omega_r}\right)}{\cos\left(\frac{\omega\pi}{2\omega_r}\right)} \sin\left(\frac{\ell_r^s \omega}{v}\right) \right] \Bigg|_{\omega \rightarrow \omega_r}, \quad (\text{C6})$$

$$A_p = \left[\frac{\left(\frac{\omega_p}{\omega} - \frac{\omega}{\omega_p}\right)}{\cos\left(\frac{\omega\pi}{2\omega_p}\right)} \sin\left(\frac{\ell_p^s \omega}{v}\right) \right] \Bigg|_{\omega \rightarrow \omega_p}. \quad (\text{C7})$$

Evaluating the factors yields

$$\tilde{C}_J \approx C_J \sin\left(\frac{\ell_r^s \omega_r}{v}\right) \sin\left(\frac{\ell_p^s \omega_p}{v}\right). \quad (\text{C8})$$

According to this approximation, the equivalent-circuit capacitance vanishes as the distributed-circuit capacitor approaches the shorted end of either $\lambda/4$ resonator and takes its maximum value when the distributed-circuit capacitor is connected to the open end of both resonators, in which case $\tilde{C}_J = C_J$.

The equivalent lumped-element circuit in Fig. A6(c) is solved by the branch-flux method [56, 57] to yield the following interaction Hamiltonian between the readout-resonator and dedicated-filter modes under the rotating-wave approximation,

$$\hat{\mathcal{H}}_{\text{int}} = \hbar J^{\text{cap}} (\hat{a}_r^\dagger \hat{a}_p + \hat{a}_r \hat{a}_p^\dagger), \quad (\text{C9})$$

$$J^{\text{cap}} = \frac{1}{2} \sqrt{Z_r Z_p} \omega_r \omega_p \tilde{C}_J. \quad (\text{C10})$$

The solution is valid assuming weak coupling between the modes such that $\tilde{C}_J \ll C_r, C_p$. Substituting in Eq. (C3) for the characteristic impedances $Z_{r(p)}$ and Eq. (C8) for the capacitance \tilde{C}_J yields

$$J^{\text{cap}} = \frac{2}{\pi} Z_0 \omega_r \omega_p C_J \sin\left(\frac{\omega_r \ell_r^s}{v}\right) \sin\left(\frac{\omega_p \ell_p^s}{v}\right). \quad (\text{C11})$$

This expression gives the coupling strength J^{cap} purely in terms of the distributed-circuit parameters.

2. MTL coupling

Figure A6(d) depicts the equivalent circuit for the MTL-coupled $\lambda/4$ resonators. The form of the circuit is motivated as the coupling capacitance C_n and coupling inductance L_n destructively interfere, resulting in a notch frequency where transmission through the coupled resonators is suppressed. To determine a mapping for the coupling elements C_n and L_n , we match the transfer impedance Z_{21}^{ec} for the equivalent circuit with the transfer impedance Z_{21} for the distributed circuit in Fig. A6(b) [given by Eq. (B11)] around the notch frequency ω_n . We equate both the zeroth- and first-order derivatives,

$$Z_{21}^{\text{ec}}(\omega_n) = Z_{21}(\omega_n) = 0, \quad (\text{C12})$$

$$\left. \frac{dZ_{21}^{\text{ec}}(\omega)}{d\omega} \right|_{\omega=\omega_n} = \left. \frac{dZ_{21}(\omega)}{d\omega} \right|_{\omega=\omega_n}. \quad (\text{C13})$$

The first equation gives the condition $\sqrt{L_n C_n} = 1/\omega_n$, and the second equation gives the condition

$$Z_n \equiv \sqrt{\frac{L_n}{C_n}} = Z_0 \frac{64}{\pi^3} \frac{\cos\left(\frac{\pi\omega_n}{2\omega_r}\right) \cos\left(\frac{\pi\omega_n}{2\omega_p}\right)}{\left(\frac{\omega_r}{\omega_n} - \frac{\omega_n}{\omega_r}\right) \left(\frac{\omega_p}{\omega_n} - \frac{\omega_n}{\omega_p}\right)} \frac{(c/c_m)}{\sin\left(\frac{\omega_n \ell_a}{v}\right)}. \quad (\text{C14})$$

The effective Hamiltonian of the MTL-coupled resonators can now be found because the Hamiltonian of the equivalent lumped-element circuit can be constructed following a standard procedure [56, 57]. The external flux Φ_{ext} through the inductive loop is set to zero, as the

distributed circuit from which the equivalent circuit is constructed has no such inductive loop. Focusing on the interaction part of the Hamiltonian and making the RWA yields

$$\hat{\mathcal{H}}_{\text{int}} = \hbar J (\hat{a}_r^\dagger \hat{a}_p + \hat{a}_r \hat{a}_p^\dagger), \quad (\text{C15})$$

$$J = \frac{\sqrt{Z_r Z_p}}{2Z_n} \sqrt{\omega_r \omega_p} \left(\frac{\sqrt{\omega_r \omega_p}}{\omega_n} - \frac{\omega_n}{\sqrt{\omega_r \omega_p}} \right). \quad (\text{C16})$$

The solution is valid assuming weak coupling between the modes such that $C_n \ll C_r, C_p$ and $L_n \gg L_r, L_p$. The solutions to $Z_{r(p)}$ and Z_n given in Eqs. (C3) and (C14) respectively are substituted into this expression. In addition, we make the change of variables $\omega_r = \bar{\omega}_{rp} + \Delta_{rp}/2$ and $\omega_p = \bar{\omega}_{rp} - \Delta_{rp}/2$, where $\bar{\omega}_{rp}$ is the average of the resonator and filter frequencies and Δ_{rp} is the detuning. Expanding in orders of the term Δ_{rp}/ω_n yields

$$J = \bar{\omega}_{rp} \frac{\pi^2}{32} \frac{\left(\frac{\bar{\omega}_{rp}}{\omega_n} - \frac{\omega_n}{\bar{\omega}_{rp}}\right)^3}{\cos^2\left(\frac{\pi\omega_n}{2\bar{\omega}_{rp}}\right)} \left(\frac{c_m}{c}\right) \sin\left(\frac{\omega_n \ell_c}{v}\right) + \mathcal{O}\left[\left(\frac{\Delta_{rp}}{\omega_n}\right)^2\right]. \quad (\text{C17})$$

For readout applications it is typically desirable to make the detuning Δ_{rp} as small as possible and so the higher order terms can be neglected. This results in Eq. (4) in the main text, which gives the exchange coupling strength between two MTL-coupled $\lambda/4$ resonators in terms of the resonator frequencies, the notch frequency, and the length and coupling capacitance of the MTL-coupler.

Appendix D: Circuit models for the Purcell-limited relaxation time

In this section, the circuit models used to predict the Purcell-limited qubit relaxation time T_1^{pl} are described. The models are then used to derive an expression for the Purcell-filtering enhancement provided by the intrinsic notch filter.

Figure A7 shows the general circuit used to model the energy relaxation of the qubit due to its coupling to the readout line. The qubit, with shunt capacitance C_q , is coupled via a capacitor with capacitance C_{qr} to a lossless 2-port network. The network is coupled at port 2 to a readout line with characteristic impedance Z_0 via a capacitor with capacitance C_{ext} . The characteristic relaxation time of the qubit imposed by its coupling to the readout line can be modeled by the following equation [58],

$$T_1^{\text{pl}}(\omega_q) = \frac{C_q}{\text{Re}[Y_{\text{in}}(\omega_q)]}. \quad (\text{D1})$$

Defining Z_{11} , Z_{22} , and Z_{21} as the impedance matrix elements for the lossless 2-port network, the real part of the

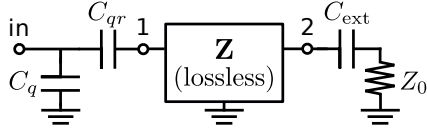


FIG. A7. Circuit model for determining the Purcell-limited relaxation time of a qubit. A qubit with shunt capacitance C_q is capacitively coupled to port 1 of a lossless 2-port network with impedance matrix \mathbf{Z} . Port 2 of the network is capacitively coupled to a load with resistance Z_0 .

input admittance Y_{in} for the circuit in Fig. A7 is given by

$$\text{Re}[Y_{\text{in}}(\omega)] = \frac{Z_0 |Z_{21}|^2}{|(Z_{11} + Z_{qr})(Z_{22} + Z_{\text{ext}} + Z_0)|^2}, \quad (\text{D2})$$

$$Z_{qr} = \frac{-i}{\omega C_{qr}}, \quad Z_{\text{ext}} = \frac{-i}{\omega C_{\text{ext}}}. \quad (\text{D3})$$

This expression is valid when $Z_{21} \ll Z_{11}, Z_{22}$. The transfer impedances Z_{21} for the 2-port network given the specific circuits shown in Figs. A6(c) and (d) are defined as Z_{21}^{cap} and Z_{21}^{MTL} , respectively. Likewise, the Purcell-limited relaxation times of the qubit given these specific circuits are defined as T_1^{cap} and T_1^{MTL} .

The predicted Purcell-limited relaxation times plotted in Fig. 5(b) of the main text were generated using T_1^{cap} and T_1^{MTL} . The circuit parameters were constrained to match the measured frequencies, coupling strengths and external linewidths for the qubit and the readout and filter resonators, in a similar manner to Ref. 30. For completeness, the shunting impedance to ground given by Eq. (E7) in Appendix E was included in the model. The effect of the shunt impedance is the following adjustment to the values of Z_{ext} and Z_0 ,

$$Z_{\text{ext}} \rightarrow Z_{\text{ext}} + \frac{Z_{\text{shunt}}}{1 + |Z_{\text{shunt}}/Z_0|^2}, \quad (\text{D4})$$

$$Z_0 \rightarrow \frac{Z_0}{1 + |Z_0/Z_{\text{shunt}}|^2}. \quad (\text{D5})$$

Including the shunt impedance in the model results in a modest increase in the Purcell-limited relaxation times at the qubit frequencies of around 5 to 10%.

For weak coupling between the readout resonator and dedicated filter and at frequencies away from their resonances, Z_{11} and Z_{22} are to a good approximation independent of the coupling-circuit implementation such that $Z_{11}^{\text{cap}} = Z_{11}^{\text{MTL}}$ and $Z_{22}^{\text{cap}} = Z_{22}^{\text{MTL}}$. As a result, the ratio of the relaxation times takes the form

$$\frac{T_1^{\text{MTL}}(\omega_q)}{T_1^{\text{cap}}(\omega_q)} = \left| \frac{Z_{21}^{\text{cap}}(\omega_q)}{Z_{21}^{\text{MTL}}(\omega_q)} \right|^2. \quad (\text{D6})$$

Given that the readout resonator and dedicated filter are weakly coupled, this reduces to

$$\frac{T_1^{\text{MTL}}(\omega_q)}{T_1^{\text{cap}}(\omega_q)} = \left[\frac{\omega_q Z_n \tilde{C}_J}{\left(\frac{\omega_n}{\omega_q} - \frac{\omega_q}{\omega_n}\right)} \right]^2. \quad (\text{D7})$$

Using Eqs. (C10) and (C16) from Appendix C, the parameters \tilde{C}_J and Z_n can be expressed in terms of the coupling strengths J^{cap} and J^{MTL} , respectively, yielding

$$\tilde{C}_J = \frac{\pi J^{\text{cap}}}{2Z_0 \bar{\omega}_{rp}^2} + \mathcal{O} \left[\left(\frac{\Delta_{rp}}{\bar{\omega}_{rp}} \right)^2 \right], \quad (\text{D8})$$

$$Z_n = \frac{2}{\pi} Z_0 \left(\frac{\bar{\omega}_{rp}}{\omega_n} - \frac{\omega_n}{\bar{\omega}_{rp}} \right) \frac{\bar{\omega}_{rp}}{J^{\text{MTL}}} + \mathcal{O} \left[\left(\frac{\Delta_{rp}}{\omega_n} \right)^2 \right]. \quad (\text{D9})$$

Dropping the higher-order terms and substituting these expressions into Eq. (D7) expresses the ratio of the relaxation times in terms of frequencies and coupling strengths. The coupling strengths J^{cap} and J^{MTL} are then equated so as to ensure a fair comparison between the T_1 limits, yielding

$$\frac{T_1^{\text{MTL}}(\omega_q)}{T_1^{\text{cap}}(\omega_q)} = \frac{1}{4} \frac{\omega_q^2}{\Delta_{qn}^2} \left(1 - \frac{\omega_n^2}{\bar{\omega}_{rp}^2} \right)^2 \left(1 + \mathcal{O} \left[\left(\frac{\Delta_{qn}}{\omega_n} \right)^2 \right] \right), \quad (\text{D10})$$

where $\Delta_{qn} = \omega_q - \omega_n$ is the detuning of the qubit from the notch. Dropping the higher-order terms and defining $\xi \equiv T_1^{\text{MTL}}(\omega_q)/T_1^{\text{cap}}(\omega_q)$ results in Eq. (5) in the main text.

Appendix E: Semi-classical model for the readout system dynamics

This section describes the semi-classical model for the multiplexed readout and filter resonators. The model is utilized to predict both the steady-state and time-dependent responses of the readout system to an external drive, and to determine the system's normal modes.

Figure A8 shows the input-output network used to model the multiplexed readout system. A traveling coherent field s_{in} propagating along a transmission line with characteristic impedance Z_0 is incident on the system of coupled readout and filter resonators. The traveling fields are treated classically when considering their behavior at the shunt and at the node where the fields scatter. They are treated using input-output theory [59] when considering their interaction with the resonators. We denote the coherent field amplitudes of filter resonator j and readout resonator j as p_j and r_j , respectively. The term $\kappa_{p,j}$ is the external linewidth of filter mode j , and the term J_j is the coupling strength between filter resonator j and readout resonator j . The model is linear, and qubits are treated as only inducing a state-dependent shift to the readout-resonator frequencies.

The reflection coefficient of the incident field is defined by

$$\Gamma_{\text{incident}} \equiv \frac{s_{\text{out}}}{s_{\text{in}}}. \quad (\text{E1})$$

The incident field is treated as separating into distinct fields that each interact with a single filter mode or with

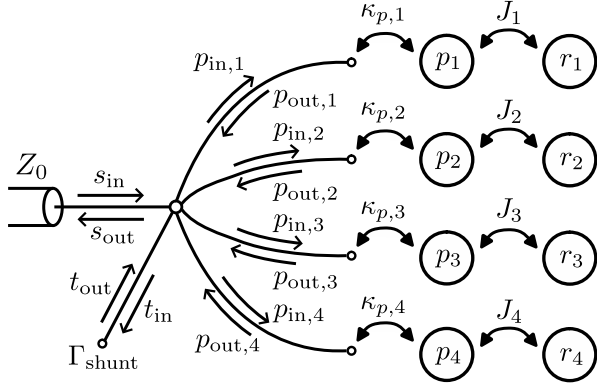


FIG. A8. Input–output network for the multiplexed system of four readout resonators of amplitudes r_j and dedicated filter resonators of amplitudes p_j ($j = 1, \dots, 4$). The multiplexed resonators couple to the end of a transmission line with characteristic impedance Z_0 . The model is generalized to include a shunt impedance to ground.

the shunt. The incoming and outgoing fields at the node where the separation occurs obey the relations

$$s_{\text{out}} - s_{\text{in}} = t_{\text{out}} - t_{\text{in}} + \sum_{j=1}^4 (p_{\text{out},j} - p_{\text{in},j}), \quad (\text{E2})$$

$$s_{\text{out}} + s_{\text{in}} = t_{\text{out}} + t_{\text{in}} = p_{\text{out},j} + p_{\text{in},j}. \quad (\text{E3})$$

These conditions result from Kirchoff's laws. The fields incident at the shunt and the filter resonators are reflected with reflection coefficients defined by

$$\Gamma_{\text{shunt}} \equiv \frac{t_{\text{out}}}{t_{\text{in}}}, \quad \Gamma_{p,j} \equiv \frac{p_{\text{out},j}}{p_{\text{in},j}}. \quad (\text{E4})$$

Combining Eqs. (E1)–(E4) yields the following solution for the reflection coefficient of an incident readout signal,

$$\frac{1 - \Gamma_{\text{incident}}}{1 + \Gamma_{\text{incident}}} = \frac{1 - \Gamma_{\text{shunt}}}{1 + \Gamma_{\text{shunt}}} + \sum_{j=1}^4 \left(\frac{1 - \Gamma_{p,j}}{1 + \Gamma_{p,j}} \right). \quad (\text{E5})$$

We note that this expression is equivalent to stating that the total load impedance terminating the transmission line is the parallel sum of the shunt impedance and the readout-circuit impedance.

The reflection coefficient at the shunt is given by

$$\Gamma_{\text{shunt}} = \frac{Z_{\text{shunt}} - Z_0}{Z_{\text{shunt}} + Z_0}. \quad (\text{E6})$$

Here, the shunt impedance Z_{shunt} takes the form of a parallel LC resonator

$$\frac{1}{Z_{\text{shunt}}} = -\frac{i}{\omega L_{\text{shunt}}} + i\omega C_{\text{shunt}}. \quad (\text{E7})$$

The term C_{shunt} is the parasitic shunt capacitance of the TSV structure that routes signals from the pogo pin on the circuit backside to the filter resonators, and L_{shunt} is

due to the backside spiral inductance that connects the TSV structure to the ground plane [Figs. 4(e) and A1(c)]. Shunt values of $C_{\text{shunt}} = 230$ fF and $L_{\text{shunt}} = 1.01$ nH were determined by COMSOL simulations and an analytic formula for the inductance of a spiral inductor [60]. At the frequency $1/\sqrt{L_{\text{shunt}}C_{\text{shunt}}} = 10.44$ GHz, the shunt impedance goes to infinity and thus the reflection coefficient Γ_{shunt} approaches 1. As a result, around the readout frequencies, the effect of the large shunt capacitance is screened out by the shunt inductance. Using input–output theory [59], the incident and reflected fields at the filter resonators are related to the coherent field amplitudes of the filter resonators by the expression

$$p_{\text{out},j} = p_{\text{in},j} - \sqrt{\kappa_{p,j}} p_j. \quad (\text{E8})$$

The equations of motion for the coupled filter-mode and readout-resonator-mode system are given by

$$\frac{dp_j}{dt} = -i\Delta_{pd,j} p_j - \frac{\kappa_{p,j} + \gamma_{p,j}}{2} p_j - iJ_j r_j + \sqrt{\kappa_{p,j}} p_{\text{in},j}, \quad (\text{E9})$$

$$\frac{dr_j}{dt} = -i\Delta_{rd,j}^{g(e)} r_j - \frac{\gamma_{r,j}}{2} r_j - iJ_j p_j. \quad (\text{E10})$$

Here, $\Delta_{pd,j} = \omega_{p,j} - \omega_d$ is the detuning of filter mode j from the drive, $\Delta_{rd,j}^{g(e)} = \omega_{r,j}^{g(e)} - \omega_d$ is the qubit-state-dependent detuning of readout mode j from the drive, and $\omega_{r,j}^e = \omega_{r,j}^g + 2\chi_j$ is the readout-mode frequency given the qubit is in the $|e\rangle$ state. The terms $\gamma_{r,j}$ and $\gamma_{p,j}$ are the internal linewidths of readout resonator j and filter resonator j , respectively.

1. Steady-state results

Solving the equations of motion in the steady state and combining with Eq. (E8) yields the following solution for the qubit-state-dependent reflection coefficients at the dedicated filters

$$\Gamma_{p,j}^{g(e)} = 1 - \frac{4i\kappa_{p,j} \left(\Delta_{rd,j}^{g(e)} - i\gamma_{r,j}/2 \right)}{(2i\Delta_{pd,j} + \kappa_{p,j} + \gamma_{p,j}) \left(2i\Delta_{rd,j}^{g(e)} + \gamma_{r,j} \right) + 4J_j^2}. \quad (\text{E11})$$

By combining this result with Eq. (E6) for the reflection coefficient at the shunt, the steady-state reflection at the device given by Eq. (E5) is fully determined from the readout and shunt parameters. An important detail is that input–output theory uses the clockwise sign convention for phasor rotation whereas Eq. (E7) for the shunt impedance uses the counterclockwise convention from electrical engineering. When fitting to the measured data we choose the electrical engineering convention and so all values of i in Eq. (E11) are replaced with $-i$. The measured reflection response Γ_{meas} was fit to the model function

$$\arg(\Gamma_{\text{meas}}) = \arg(\Gamma_{\text{incident}}) + \theta_0 - \omega\tau. \quad (\text{E12})$$

Here, θ_0 is a constant phase offset, and τ accounts for the electrical length of the experimental setup. The reflection spectrum Γ_{meas} was measured twice over a frequency range that covered all of the readout-resonator and filter-resonator modes; first with all qubits prepared in the $|g\rangle$ state and then with all qubits prepared in the $|e\rangle$ state. The two datasets were then fit simultaneously to extract the parameters $\omega_{r,j}$, $\omega_{p,j}$, $\kappa_{p,j}$, J_j and χ_j for all the filter resonators and readout resonators. The parameters $\gamma_{p,j}$ and $\gamma_{r,j}$ were set to zero in the model function since the external decay rates of the filter resonators dominated over all the internal decay rates. The bare readout-resonator and filter-resonator parameters extracted from the fit are presented in Table AII.

The bounds on the noise-photon populations $n_{r,j}^{\text{noise}}$ of readout-resonators given in the main text were determined from the fitted parameters using the relation [18]

$$\Gamma_{\phi,j}^{\text{noise}} = \frac{n_{r,j}^{\text{noise}}}{2} \int_{-\infty}^{\infty} |\Gamma_{\text{incident}}^e(\omega) - \Gamma_{\text{incident}}^g(\omega)|^2 \frac{d\omega}{2\pi}, \quad (\text{E13})$$

where $\Gamma_{\phi,j}^{\text{noise}}$ is the noise-photon-induced dephasing rate in qubit j and $\Gamma_{\text{incident}}^{g(e)}(\omega)$ is the reflection coefficient at the device when qubit j is in the $|g\rangle$ and $|e\rangle$ states, respectively.

2. Time-dependent results

In order to solve the time dependence of the coherent field amplitudes, it is convenient to use a matrix representation. The driven system of coupled readout and filter resonators can be expressed by the matrix equation

$$\frac{d}{dt} \begin{pmatrix} \mathbf{p} \\ \mathbf{r} \end{pmatrix} = -i \begin{pmatrix} \mathbf{P} & \mathbf{J} \\ \mathbf{J} & \mathbf{R}^{g(e)} \end{pmatrix} \begin{pmatrix} \mathbf{p} \\ \mathbf{r} \end{pmatrix} + \begin{pmatrix} \mathbf{d} \\ \mathbf{0} \end{pmatrix} s_{\text{in}}. \quad (\text{E14})$$

Here, \mathbf{P} is a 4×4 matrix for the filter-resonators, \mathbf{J} is a 4×4 matrix for the couplings between the filter-resonator and readout-resonator modes, and $\mathbf{R}^{g(e)}$ is a qubit-state-dependent 4×4 matrix for the readout-resonators. The terms \mathbf{p} and \mathbf{r} are the field amplitudes for the filter resonators and readout resonators, respectively given by

$$\mathbf{p} = \begin{pmatrix} p_1 \\ p_2 \\ p_3 \\ p_4 \end{pmatrix}, \quad \mathbf{r} = \begin{pmatrix} r_1 \\ r_2 \\ r_3 \\ r_4 \end{pmatrix}, \quad (\text{E15})$$

and \mathbf{d} gives the coupling coefficients of the driving field s_{in} to the filter resonators,

$$\mathbf{d} = \left(\frac{1 + \Gamma_{\text{shunt}}}{2} \right) \begin{pmatrix} \sqrt{\kappa_{p,1}} \\ \sqrt{\kappa_{p,2}} \\ \sqrt{\kappa_{p,3}} \\ \sqrt{\kappa_{p,4}} \end{pmatrix}. \quad (\text{E16})$$

The matrix \mathbf{P} has elements given by

$$\mathbf{P}_{ij} = \left(\Delta_{pd,i} - i \frac{\gamma_{p,i}}{2} \right) \delta_{ij} - i \frac{\sqrt{\kappa_{p,i} \kappa_{p,j}}}{4} (1 + \Gamma_{\text{shunt}}), \quad (\text{E17})$$

where δ_{ij} is the Kronecker delta function. The second term introduces off-diagonal elements to the matrix \mathbf{P} , which represent coupling between the different filter modes. This is due to the fact that the filter resonators all couple to the readout line via a shared node. The matrix \mathbf{J} is diagonal with elements given by

$$\mathbf{J}_{ij} = J_i \delta_{ij}. \quad (\text{E18})$$

This matrix couples filter-resonator amplitude p_j to readout-resonator amplitude r_j with coupling strength J_j . Finally, the matrix $\mathbf{R}^{g(e)}$ is diagonal with elements given by

$$\mathbf{R}_{ij}^{g(e)} = \left(\Delta_{rd,i}^{g(e)} - i \frac{\gamma_{r,i}}{2} \right) \delta_{ij}. \quad (\text{E19})$$

This matrix contains all of the qubit-state dependence and has 16 different permutations depending on the four-qubit state. The system of coupled first-order differential equations in Eq. (E14) can be solved numerically to find the time evolution of the coherent field amplitudes of the readout and filter resonators under a drive. The time-dependent output field $s_{\text{out}}(t)$ into the transmission line is then determined from the filter-resonator amplitudes through Eqs. (E2), (E3) and (E8), yielding

$$s_{\text{out}}(t) = \Gamma_{\text{shunt}} s_{\text{in}}(t) - \left(\frac{1 + \Gamma_{\text{shunt}}}{2} \right) \sum_{j=1}^4 \sqrt{\kappa_{p,j}} p_j(t). \quad (\text{E20})$$

As a result, the output-field separation $S(t) \equiv |s_{\text{out}}^e(t) - s_{\text{out}}^g(t)|$ for a readout drive targeting qubit j is to a good approximation given by

$$S(t) = \left| \frac{1 + \Gamma_{\text{shunt}}}{2} \right| \sqrt{\kappa_{p,j}} |p_j^e(t) - p_j^g(t)|. \quad (\text{E21})$$

The predicted output-field separation using this expression is plotted in Fig. 7(a) of the main text for a readout drive targeting qubit Q_2 .

3. Normal modes

In the absence of an external drive, the eigenvalues $\tilde{\lambda}_k$ ($k = 1, \dots, 8$) of Eq. (E14) give the normal modes of the coupled readout and filter resonators. Here, we set $\Gamma_{\text{shunt}} = 1$, as this is a good approximation around the readout- and filter-resonator frequencies and it simplifies finding the eigenvalues. The frequencies and effective external linewidths of the normal modes are then given by

$$\tilde{\omega}_k = \text{Re}(\tilde{\lambda}_k), \quad \tilde{\kappa}_k = -2\text{Im}(\tilde{\lambda}_k). \quad (\text{E22})$$

The eight normal modes are separated into pairs, each corresponding to the hybridized modes of a particular readout-resonator and filter-resonator pair. This picture is a slight simplification of the true nature of these modes,

TABLE AII. Bare readout parameters. Here, g is the coupling strength between the qubit and the readout resonator, and n_{crit} is the critical photon number of the readout resonator.

	$\omega_r^g/2\pi$ (MHz)	$\omega_p/2\pi$ (MHz)	$J/2\pi$ (MHz)	$\kappa_p/2\pi$ (MHz)	$\chi/2\pi$ (MHz)	$g/2\pi$ (MHz)	n_{crit}
Q ₁	10250	10232	36.1	97.6	-9.4	420	7.0
Q ₂	10386	10407	39.4	81.4	-9.9	423	6.7
Q ₃	10540	10566	30.9	66.7	-10.5	280	7.1
Q ₄	10666	10710	26.2	93.5	-8.3	275	9.4

since in reality the coupling between the filter resonators means the normal modes hybridize across the whole network of resonators. However, by looking at the qubit-state dependence it is clear that each normal mode can be associated with a particular readout-resonator and filter-resonator pair. The dispersive shifts due to a target qubit were found by solving the normal modes for the $|g\rangle$ and $|e\rangle$ states of the target qubit with all other qubits in the ground state and using the standard definition $\tilde{\chi}_r \equiv (\tilde{\omega}_r^e - \tilde{\omega}_r^g)/2$. The dispersive shift induced in spectator normal modes (mediated via the coupling of the filter resonators) was in all cases less than 1% of the shift in the target normal mode.

The normal modes are summarized in Table AIII. Here, $\tilde{\omega}_r^{g(e)}$ denotes the readout-resonator-like modes and $\tilde{\omega}_p^{g(e)}$ the filter-resonator-like modes. By definition, the readout-resonator-like modes have smaller external linewidths and larger dispersive shifts than the corresponding filter-resonator-like modes. For the readout characterization, measurement was performed by driving the readout-resonator-like modes, as this resulted in superior SNR. As a result, we refer to these modes as the readout modes and $\tilde{\omega}_r^g$, $\tilde{\kappa}_r^g$, $\tilde{\chi}_r$ in Table AIII correspond to ω_{ro}^g , κ_{ro}^g , χ_{ro} in Table I of the main text.

Appendix F: ac-Stark-shift spectroscopy measurement

In order to calibrate the drive power incident on the device we followed the protocol in Ref. [17]. We first applied a continuous drive tone to the readout resonator of a particular qubit, in order to induce an ac Stark shift. We subsequently applied a π -pulse to the qubit followed by qubit measurement. The experiment was then repeated while sweeping the frequency ω_d of the π -pulse. The value of ω_d which results in the maximum qubit population exchange from the $|g\rangle$ to the $|e\rangle$ state is associated with the ac-Stark-shifted qubit frequency. The steady-state average photon number $n_{r,j}^g$ in readout resonator j is then inferred from the ac Stark shift Δ_{ac} through the relation $\Delta_{\text{ac}} = 2\chi_j n_{r,j}^g$ [37]. This photon number is related to the readout-resonator coherent field amplitude r_j^g by the expression $n_{r,j}^g = |r_j^g|^2$. The equations of motion Eqs. (E9) and (E10) are solved in the steady state

TABLE AIII. Normal modes of the composite readout-resonator and filter-resonator system. The terms $\tilde{\chi}_{r(p)}$ are the dispersive shifts of the normal modes defined $\tilde{\omega}_{r(p)}^e \equiv \tilde{\omega}_{r(p)}^g + 2\tilde{\chi}_{r(p)}$.

	$\tilde{\omega}_r^g/2\pi$ (MHz)	$\tilde{\omega}_p^g/2\pi$ (MHz)	$\tilde{\kappa}_r^g/2\pi$ (MHz)	$\tilde{\kappa}_r^e/2\pi$ (MHz)	$\tilde{\kappa}_p^g/2\pi$ (MHz)	$\tilde{\chi}_r/2\pi$ (MHz)	$\tilde{\chi}_p/2\pi$ (MHz)
Q ₁	10221	10284	42	30	42	-5.9	-3.5
Q ₂	10360	10438	34	25	63	-7.8	-2.3
Q ₃	10520	10582	24	14	55	-8.4	-2.3
Q ₄	10652	10701	19	11	59	-7.2	-1.1

to find the input field on the filter resonator $p_{\text{in},j}$ as a function of r_g . Finally, the incident field on the device is determined from the incident field on the filter resonator using the relation

$$\frac{s_{\text{in}}}{p_{\text{in},j}} = \frac{1 + \Gamma_{p,j}}{1 + \Gamma_{\text{incident}}}. \quad (\text{F1})$$

Here, Γ_{incident} and $\Gamma_{p,j}$ are the reflection coefficients defined in Appendix E, which are determined from the readout and shunt parameters. The squared norm of the incident field $|s_{\text{in}}|^2$ corresponds to the photon flux \dot{n} on the device, and thus the power incident on the device is given by $P = \hbar\omega_d |s_{\text{in}}|^2$.

From the calibrated power incident on the device, we could determine the attenuation between the generator and the device. We make the assumption that this attenuation is the same over the range of frequencies that are driven in the subsequent section. Since the attenuation of the coaxial cables of the input lines increases with frequency, this assumption will lead to lower-bound values for the Purcell-limited relaxation time.

Next, the drive amplitude Ω incident on the qubit was determined as a function of frequency. Here, Ω is defined in terms of the drive Hamiltonian as $\hat{\mathcal{H}}_{\text{drive}} = \hbar\Omega (a_q^\dagger + a_q) \cos(\omega_d t)$ where a_q^\dagger and a_q are the creation and annihilation operators for the qubit.

As described in the main text, Ω was determined by two methods following Ref. 16: (i) by measuring the Rabi frequencies of the qubit when driving at the $|g\rangle$ - $|e\rangle$ and $|e\rangle$ - $|f\rangle$ transition frequencies, and (ii) by measuring the induced ac Stark shift Δ_{ac} in the qubit when detuned from these transitions. The drive is applied through the readout line. Figures A9(a) and (b) show Rabi oscillations in Q₁. The $|g\rangle$ - $|e\rangle$ and $|e\rangle$ - $|f\rangle$ Rabi oscillation frequencies are equal to Ω and $\sqrt{2}\Omega$, respectively.

Figure A9(c) shows the measured ac Stark shift Δ_{ac} normalized by the incident power for qubit Q₂ as a function of the drive frequency. The drive amplitude Ω was then determined from the measured ac Stark shift using the perturbative formula in Ref. 16. The results are sensitive to the calibrated value of the qubit frequency ω_q . We determined this more precisely by applying a Stark shifting drive to the qubit over a range of powers P , and performing a linear fit of the Stark-shifted qubit frequency $\omega_{q,\text{ac}}$ to the formula $\omega_{q,\text{ac}} = \omega_q + kP$, where k

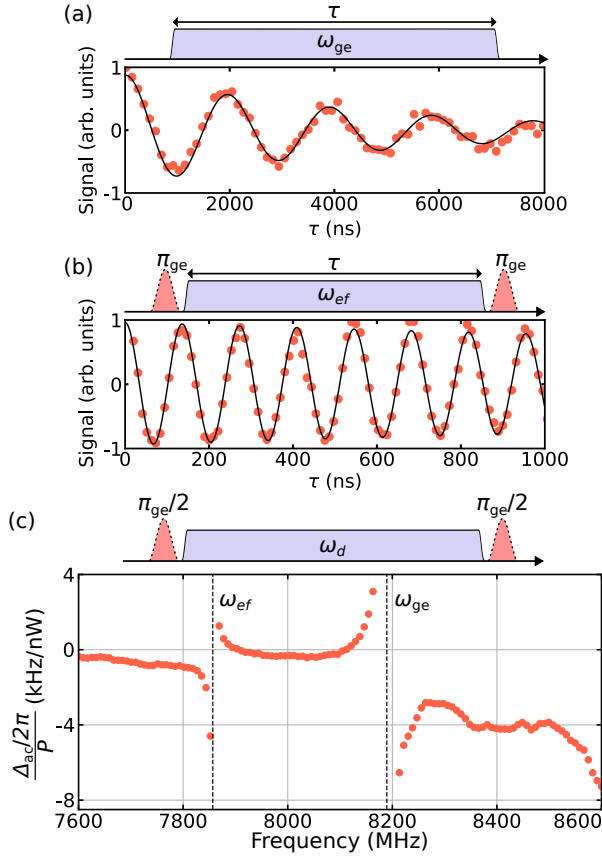


FIG. A9. (a)–(b) Rabi oscillations in qubit Q_1 driven at the $|g\rangle$ – $|e\rangle$ and the $|e\rangle$ – $|f\rangle$ transition frequencies, respectively. (c) Pulse sequence for measuring the ac Stark shift and results for qubit Q_2 . The ratio between the Stark shift and incident power P as a function of drive frequency.

is the slope of the linear fit. From the fit, we extracted the value of ω_q and an associated uncertainty.

In qubits Q_1 , Q_2 and Q_3 , we observed a frequency range between the $|g\rangle$ – $|e\rangle$ and $|e\rangle$ – $|f\rangle$ transition frequencies where the drive induced a small negative ac Stark shift in the qubit—contrary to the positive shift that is expected across this frequency range. This may result from spurious harmonics of the generator producing the Stark shifting drive, since the sensitivity to the main drive tone is strongly suppressed around the notch frequency. We excluded the data in this range when determining the Purcell-limited relaxation time.

From the measured drive amplitude and the incident power, the Purcell-limited relaxation time of the qubit is given by [16]

$$T_1^{\text{pl}}(\omega_d) = \frac{4P}{\Omega^2 \hbar \omega_d}. \quad (\text{F2})$$

TABLE AIV. Further information regarding the readout. Here, σ_e/σ_g expresses the ratio of the readout signal standard deviations for the $|g\rangle$ and $|e\rangle$ states. The terms $P_0(e_2|g_1)$ and $P_\pi(g_2|g_1)$ are the error contributions to the assignment fidelity when the qubit was prepared in the $|g\rangle$ and $|e\rangle$ states, respectively. The term P_e is the excited-state population of the qubits prior to state-preparation, and ω_d is the drive frequency that was used to perform readout.

	SNR	σ_e/σ_g	$P_0(e_2 g_1)$ (%)	$P_\pi(g_2 g_1)$ (%)	P_e (%)	$\omega_d/2\pi$ (MHz)
Q_1	6.3	1.03	0.22	0.49	1.7	10224
Q_2	8.4	0.99	0.03	0.16	2.3	10357
Q_3	6.0	1.03	0.13	0.44	1.4	10515
Q_4	6.7	0.99	0.08	0.33	1.0	10646

Appendix G: Further analysis of the fast multiplexed qubit readout

Here, further details of the fast multiplexed readout measurement are provided. First, the calculation of the separation error and coherence limited errors is discussed. The separation error was determined from the signal-to-noise ratio (SNR) of the measurements. The SNR is here defined as

$$\text{SNR} \equiv \frac{|\mu_g - \mu_e|}{(\sigma_g + \sigma_e)/2}, \quad (\text{G1})$$

where $\mu_{g(e)}$ and $\sigma_{g(e)}$ are the the mean and standard deviation, respectively, of the Gaussian fits to the $|g(e)\rangle$ state histograms shown in Fig. 7(c) of the main text. The measured SNR values for the four qubits are provided in Table AIV. The ratio σ_e/σ_g is also given, showing that the noise for the $|g\rangle$ and $|e\rangle$ states was almost the same. The separation error due to overlap of the projected Gaussian distributions is estimated from the SNR as [17, 61]

$$\varepsilon_{\text{sep}} = \frac{1}{2} \left[1 - \text{erf} \left(\frac{\text{SNR}}{\sqrt{8}} \right) \right]. \quad (\text{G2})$$

The coherence limit to the assignment fidelity is estimated as

$$\varepsilon_{\text{cl}} = \frac{\tau_{\text{meas}}}{2T_1}, \quad (\text{G3})$$

where τ_{meas} is the length of the measurement integration window. The coherence limit to the QND fidelity is estimated as

$$\varepsilon_{\text{cl}}^{\text{Q}} = \frac{\tau_{\text{buffer}}}{2T_1} + \frac{\tau_{\text{meas}}}{2T_1}, \quad (\text{G4})$$

where τ_{buffer} is the length of the buffer period between the first and second measurements of the QND measurement pulse sequence.

Figure A10 shows the IQ plots for the simultaneous measurement on the four qubits. These measurements are post-selected to ensure the qubits were prepared in the $|g\rangle$ state prior to the π pulse sequence. Table AIV

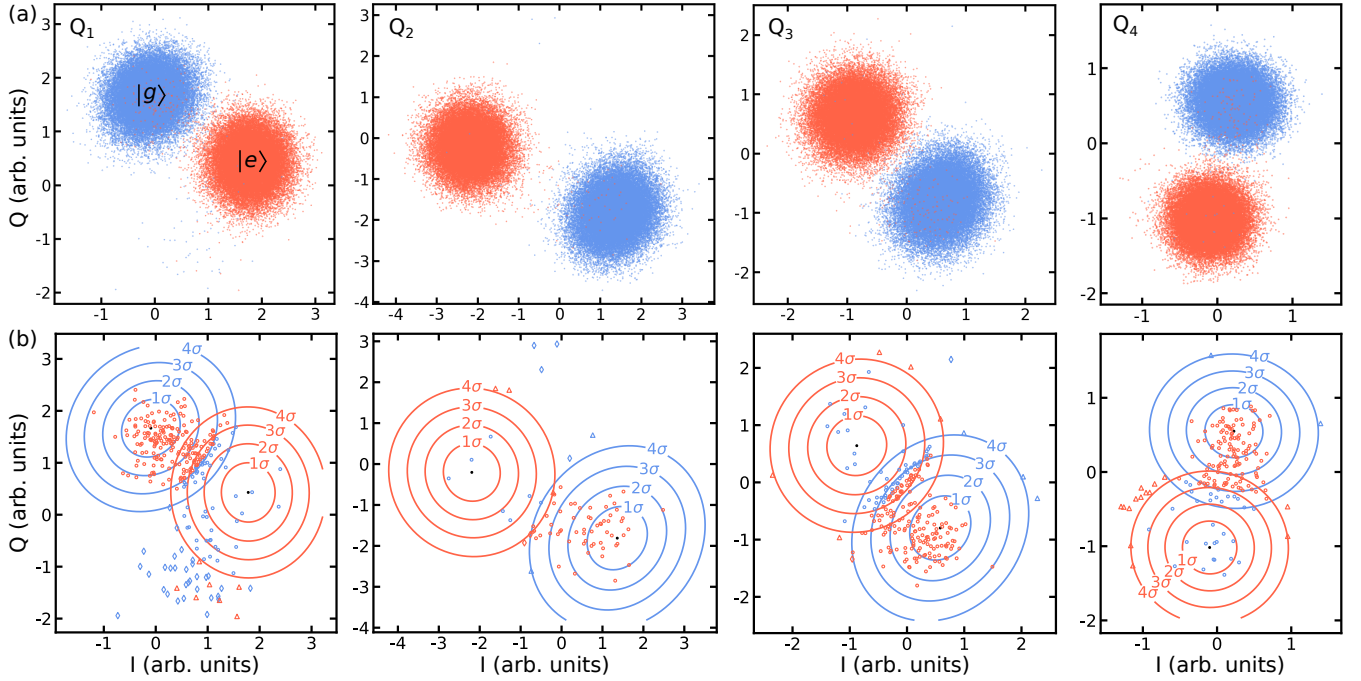


FIG. A10. Post-selected IQ signals from the assignment-fidelity pulse sequence. (a) Time-integrated IQ signals when the qubit was prepared in the $|g\rangle$ state (blue) and in the $|e\rangle$ state (red). (b) The 1σ to 4σ confidence ellipses of the fitted bivariate normal distributions. Misassigned shots that lie inside (outside) both of the 4σ ellipses are shown as circles (diamonds). Correctly assigned shots that lie outside the 4σ ellipse of the assigned state are shown as triangles.

gives the fraction of discarded measurements, represented by the excited-state population P_e . In Fig. A10(a), all of the $\sim 8 \times 10^4$ post-selected shots are plotted. We fit the measured $|g\rangle$ - and $|e\rangle$ -state data to bivariate normal distributions. From the fits, we determined the confidence ellipses. Figure A10(b) shows the 1σ (68.27%), 2σ (95.45%), 3σ (99.73%) and 4σ (99.994%) ellipses. We stress that this σ is not referring to a standard deviation. Rather, the interpretation is that 68.27% of single-shot measurements are expected to lie inside the 1σ confidence ellipse, 95.45% inside the 2σ ellipse, etc. Shots that were misassigned are highlighted. These are divided into two categories. Shots that were misassigned and that lie inside (outside) the 4σ ellipses for both the $|g\rangle$ and $|e\rangle$ states are shown as circles (diamonds). We attribute misassigned shots outside the 4σ ellipses to measurement-induced excitation to leakage states as we would not expect these events if the qubit were restricted to the $|g\rangle$ - $|e\rangle$ subspace. In addition, correctly assigned shots that

lie outside the 4σ ellipse of the assigned state are shown as triangles. We expect approximately 5 of these events across 8×10^4 measurements. When many of these events cluster together, we again attribute it to measurement-induced leakage.

For Q_1 , there is a clear signature of leakage from the $|g\rangle$ state that made a significant contribution to the assignment error. There is also a signature of leakage from the $|e\rangle$ state that did not lead to assignment errors. In the remaining qubits, $>4\sigma$ measurements with signatures of leakage affect less than 0.015% of the total measurements. However, we emphasize that the absence of high- σ events in the IQ plane does not preclude all leakage events. For instance, it is possible for the output field given the qubit is in a leakage state to overlap with the $|g\rangle$ - or $|e\rangle$ -state output fields. Further characterization such as pseudo-syndrome detection [28] could be performed in order to detect such ‘hidden’ leakage events.

-
- [1] R. Acharya, L. Aghababaie-Beni, I. Aleiner, T. I. Andersen, M. Ansmann, F. Arute, K. Arya, A. Asfaw, N. Astrakhantsev, J. Atalaya, *et al.*, Quantum error correction below the surface code threshold, arXiv preprint arXiv:2408.13687 (2024).
 [2] Suppressing quantum errors by scaling a surface code logical qubit, *Nature* **614**, 676 (2023).

- [3] Y. Zhao, Y. Ye, H.-L. Huang, Y. Zhang, D. Wu, H. Guan, Q. Zhu, Z. Wei, T. He, S. Cao, *et al.*, Realization of an error-correcting surface code with superconducting qubits, *Physical Review Letters* **129**, 030501 (2022).
 [4] S. Krinner, N. Lacroix, A. Remm, A. Di Paolo, E. Genois, C. Leroux, C. Hellings, S. Lazar, F. Swiadek, J. Herrmann, *et al.*, Realizing repeated quantum error correc-

- tion in a distance-three surface code, *Nature* **605**, 669 (2022).
- [5] J. F. Marques, B. Varbanov, M. Moreira, H. Ali, N. Muthusubramanian, C. Zachariadis, F. Battistel, M. Beekman, N. Haider, W. Vlothuizen, *et al.*, Logical-qubit operations in an error-detecting surface code, *Nature Physics* **18**, 80 (2022).
- [6] A. G. Fowler, M. Mariantoni, J. M. Martinis, and A. N. Cleland, Surface codes: Towards practical large-scale quantum computation, *Physical Review A* **86**, 032324 (2012).
- [7] N. Tantivasadakarn, R. Thorngren, A. Vishwanath, and R. Verresen, Long-range entanglement from measuring symmetry-protected topological phases, *Physical Review X* **14**, 021040 (2024).
- [8] E. H. Chen, G.-Y. Zhu, R. Verresen, A. Seif, E. Bäumer, D. Layden, N. Tantivasadakarn, G. Zhu, S. Sheldon, A. Vishwanath, *et al.*, Realizing the nishimori transition across the error threshold for constant-depth quantum circuits, arXiv preprint arXiv:2309.02863 (2023).
- [9] G.-Y. Zhu, N. Tantivasadakarn, A. Vishwanath, S. Trebst, and R. Verresen, Nishimori's cat: stable long-range entanglement from finite-depth unitaries and weak measurements, *Physical Review Letters* **131**, 200201 (2023).
- [10] T.-C. Lu, L. A. Lessa, I. H. Kim, and T. H. Hsieh, Measurement as a shortcut to long-range entangled quantum matter, *PRX Quantum* **3**, 040337 (2022).
- [11] R. Raussendorf, D. E. Browne, and H. J. Briegel, Measurement-based quantum computation on cluster states, *Physical review A* **68**, 022312 (2003).
- [12] E. Bäumer, V. Tripathi, D. S. Wang, P. Rall, E. H. Chen, S. Majumder, A. Seif, and Z. K. Mineev, Efficient long-range entanglement using dynamic circuits, *PRX Quantum* **5**, 030339 (2024).
- [13] E. Jeffrey, D. Sank, J. Mutus, T. White, J. Kelly, R. Barends, Y. Chen, Z. Chen, B. Chiaro, A. Dunsworth, *et al.*, Fast accurate state measurement with superconducting qubits, *Physical Review Letters* **112**, 190504 (2014).
- [14] T. Walter, P. Kurpiers, S. Gasparinetti, P. Magnard, A. Potočnik, Y. Salathé, M. Pechal, M. Mondal, M. Oppliger, C. Eichler, *et al.*, Rapid high-fidelity single-shot dispersive readout of superconducting qubits, *Physical Review Applied* **7**, 054020 (2017).
- [15] J. Heinsoo, C. K. Andersen, A. Remm, S. Krinner, T. Walter, Y. Salathé, S. Gasparinetti, J.-C. Besse, A. Potočnik, A. Wallraff, *et al.*, Rapid high-fidelity multiplexed readout of superconducting qubits, *Physical Review Applied* **10**, 034040 (2018).
- [16] Y. Sunada, S. Kono, J. Ilves, S. Tamate, T. Sugiyama, Y. Tabuchi, and Y. Nakamura, Fast readout and reset of a superconducting qubit coupled to a resonator with an intrinsic Purcell filter, *Physical Review Applied* **17**, 044016 (2022).
- [17] F. Swiadek, R. Shillito, P. Magnard, A. Remm, C. Hellings, N. Lacroix, Q. Ficheux, D. C. Zanuz, G. J. Norris, A. Blais, *et al.*, Enhancing dispersive readout of superconducting qubits through dynamic control of the dispersive shift: Experiment and theory, arXiv preprint arXiv:2307.07765 (2023).
- [18] Y. Sunada, K. Yuki, Z. Wang, T. Miyamura, J. Ilves, K. Matsuura, P. A. Spring, S. Tamate, S. Kono, and Y. Nakamura, Photon-noise-tolerant dispersive readout of a superconducting qubit using a nonlinear Purcell filter, *PRX Quantum* **5**, 010307 (2024).
- [19] A. P. Place, L. V. Rodgers, P. Mundada, B. M. Smitham, M. Fitzpatrick, Z. Leng, A. Premkumar, J. Bryon, A. Vrajitoarea, S. Sussman, *et al.*, New material platform for superconducting transmon qubits with coherence times exceeding 0.3 milliseconds, *Nature Communications* **12**, 1779 (2021).
- [20] P. A. Spring, S. Cao, T. Tsunoda, G. Campanaro, S. Fasciati, J. Wills, M. Bakr, V. Chidambaram, B. Shteynas, L. Carpenter, *et al.*, High coherence and low cross-talk in a tileable 3D integrated superconducting circuit architecture, *Science Advances* **8**, eabl6698 (2022).
- [21] C. Wang, X. Li, H. Xu, Z. Li, J. Wang, Z. Yang, Z. Mi, X. Liang, T. Su, C. Yang, *et al.*, Towards practical quantum computers: Transmon qubit with a lifetime approaching 0.5 milliseconds, *npj Quantum Information* **8**, 3 (2022).
- [22] H. Deng, Z. Song, R. Gao, T. Xia, F. Bao, X. Jiang, H.-S. Ku, Z. Li, X. Ma, J. Qin, *et al.*, Titanium nitride film on sapphire substrate with low dielectric loss for superconducting qubits, *Physical Review Applied* **19**, 024013 (2023).
- [23] S. Kono, J. Pan, M. Chegnizadeh, X. Wang, A. Youssefi, M. Scigliuzzo, and T. J. Kippenberg, Mechanically induced correlated errors on superconducting qubits with relaxation times exceeding 0.4 milliseconds, arXiv preprint arXiv:2305.02591 (2023).
- [24] J. Biznárová, A. Osman, E. Rehnman, L. Chayanun, C. Křižan, P. Malmberg, M. Rommel, C. Warren, P. Delsing, A. Yurgens, *et al.*, Mitigation of interfacial dielectric loss in aluminum-on-silicon superconducting qubits, arXiv preprint arXiv:2310.06797 (2023).
- [25] A. Somoroff, Q. Ficheux, R. A. Mencia, H. Xiong, R. Kuzmin, and V. E. Manucharyan, Millisecond coherence in a superconducting qubit, *Physical Review Letters* **130**, 267001 (2023).
- [26] T. Roy, S. Kundu, M. Chand, S. Hazra, N. Nehra, R. Cosmic, A. Ranadive, M. P. Patankar, K. Damle, and R. Vijay, Implementation of pairwise longitudinal coupling in a three-qubit superconducting circuit, *Physical Review Applied* **7**, 054025 (2017).
- [27] F. Pfeiffer, M. Werninghaus, C. Schweizer, N. Bruckmoser, L. Koch, N. J. Glaser, G. Huber, D. Bunch, F. X. Haslbeck, M. Knudsen, *et al.*, Efficient decoupling of a non-linear qubit mode from its environment, arXiv preprint arXiv:2312.16988 (2023).
- [28] S. Hazra, W. Dai, T. Connolly, P. D. Kurilovich, Z. Wang, L. N. Frunzio, and M. H. Devoret, Benchmarking the readout of a superconducting qubit for repeated measurements, arXiv preprint arXiv:2407.10934v1 (2024).
- [29] N. T. Bronn, E. Magesan, N. A. Masluk, J. M. Chow, J. M. Gambetta, and M. Steffen, Reducing spontaneous emission in circuit quantum electrodynamics by a combined readout/filter technique, *IEEE Transactions on Applied Superconductivity* **25**, 1 (2015).
- [30] A. Yen, Y. Ye, K. Peng, J. Wang, G. Cunningham, M. Gingras, B. M. Niedzielski, H. Stickler, K. Serniak, M. E. Schwartz, *et al.*, Interferometric Purcell suppression of spontaneous emission in a superconducting qubit, arXiv preprint arXiv:2405.10107 (2024).
- [31] C. R. Paul, *Analysis of Multiconductor Transmission Lines* (John Wiley & Sons, 2007).

- [32] S. Vallés-Sanclemente, S. van der Meer, M. Finkel, N. Muthusubramanian, M. Beekman, H. Ali, J. Marques, C. Zachariadis, H. Veen, T. Stavenga, *et al.*, Post-fabrication frequency trimming of coplanar-waveguide resonators in circuit QED quantum processors, *Applied Physics Letters* **123**, 034004 (2023).
- [33] H. Levine, A. Haim, J. S. Hung, N. Alidoust, M. Kalaei, L. DeLorenzo, E. A. Wollack, P. A. Arriola, A. Khalajheydayati, Y. Vaknin, *et al.*, Demonstrating a long-coherence dual-rail erasure qubit using tunable transmons, *Physical Review X* **14**, 011051 (2024).
- [34] G. Ghione, An efficient, CAD-oriented model for the characteristic parameters of multiconductor buses in high-speed digital GaAs ICs, *Analog Integrated Circuits and Signal Processing* **5**, 67 (1994).
- [35] COMSOL Multiphysics 6.2, <https://www.comsol.com> (2023).
- [36] Z. Chen, A. Megrant, J. Kelly, R. Barends, J. Bochmann, Y. Chen, B. Chiaro, A. Dunsworth, E. Jeffrey, J. Mutus, *et al.*, Fabrication and characterization of aluminum airbridges for superconducting microwave circuits, *Applied Physics Letters* **104**, 052602 (2014).
- [37] J. M. Gambetta, A. Blais, D. I. Schuster, A. Wallraff, L. Frunzio, J. Majer, M. H. Devoret, S. M. Girvin, and R. J. Schoelkopf, Qubit-photon interactions in a cavity: Measurement-induced dephasing and number splitting, *Physical Review A* **74**, 042318 (2006).
- [38] J. Y. Mutus, T. C. White, R. Barends, Y. Chen, Z. Chen, B. Chiaro, A. Dunsworth, E. Jeffrey, J. Kelly, A. Megrant, *et al.*, Strong environmental coupling in a Josephson parametric amplifier, *Applied Physics Letters* **104** (2014).
- [39] C. C. Bultink, B. Tarasinski, N. Haandbæk, S. Poletto, N. Haider, D. Michalak, A. Bruno, and L. DiCarlo, General method for extracting the quantum efficiency of dispersive qubit readout in circuit qed, *Applied Physics Letters* **112**, 092601 (2018).
- [40] A. Blais, A. L. Grimsmo, and A. Wallraff, Circuit quantum electrodynamics, *Reviews of Modern Physics* **93**, 025005 (2020).
- [41] F. Pedregosa, G. Varoquaux, A. Gramfort, V. Michel, B. Thirion, O. Grisel, M. Blondel, P. Prettenhofer, R. Weiss, V. Dubourg, *et al.*, Scikit-learn: Machine learning in python, *Journal of Machine Learning Research* **12**, 2825 (2011).
- [42] D. Sank, Z. Chen, M. Khezri, J. Kelly, R. Barends, B. Campbell, Y. Chen, B. Chiaro, A. Dunsworth, A. Fowler, *et al.*, Measurement-induced state transitions in a superconducting qubit: Beyond the rotating wave approximation, *Physical Review Letters* **117**, 190503 (2016).
- [43] R. Shillito, A. Petrescu, J. Cohen, J. Beall, M. Hauru, M. Ganahl, A. G. Lewis, G. Vidal, and A. Blais, Dynamics of transmon ionization, *Physical Review Applied* **18**, 034031 (2022).
- [44] M. F. Dumas, B. Groleau-Paré, A. McDonald, M. H. Muñoz-Arias, C. Lledó, B. D'Anjou, and A. Blais, Unified picture of measurement-induced ionization in the transmon, arXiv preprint arXiv:2402.06615 (2024).
- [45] P. Harrington, J. Monroe, and K. Murch, Quantum Zeno effects from measurement controlled qubit-bath interactions, *Physical Review Letters* **118**, 240401 (2017).
- [46] T. Thorbeck, Z. Xiao, A. Kamal, and L. C. Govia, Readout-induced suppression and enhancement of superconducting qubit lifetimes, *Physical Review Letters* **132**, 090602 (2024).
- [47] R. Gautier, É. Genois, and A. Blais, Optimal control in large open quantum systems: the case of transmon readout and reset, arXiv preprint arXiv:2403.14765 (2024).
- [48] M. Jerger, F. Motzoi, Y. Gao, C. Dickel, L. Buchmann, A. Bengtsson, G. Tancredi, C. Warren, J. Bylander, D. DiVincenzo, *et al.*, Dispersive qubit readout with intrinsic resonator reset, arXiv preprint arXiv:2406.04891 (2024).
- [49] P. Bertet, I. Chiorescu, G. Burkard, K. Semba, C. Harmans, D. P. DiVincenzo, and J. Mooij, Dephasing of a superconducting qubit induced by photon noise, *Physical Review Letters* **95**, 257002 (2005).
- [50] F. Yan, D. Campbell, P. Krantz, M. Kjaergaard, D. Kim, J. L. Yoder, D. Hover, A. Sears, A. J. Kerman, T. P. Orlando, *et al.*, Distinguishing coherent and thermal photon noise in a circuit quantum electrodynamical system, *Physical Review Letters* **120**, 260504 (2018).
- [51] Z. Wang, S. Shankar, Z. Mineev, P. Campagne-Ibarcq, A. Narla, and M. H. Devoret, Cavity attenuators for superconducting qubits, *Physical Review Applied* **11**, 014031 (2019).
- [52] J. Goetz, S. Pogorzalek, F. Deppe, K. Fedorov, P. Eder, M. Fischer, F. Wulschner, E. Xie, A. Marx, and R. Gross, Photon statistics of propagating thermal microwaves, *Physical Review Letters* **118**, 103602 (2017).
- [53] T. Sumida, M. Negoro, K. Ogawa, T. Miyoshi, H. Shiomi, S. Morisaka, R. Matsuda, K. Koike, S. Funada, R. Ohira, *et al.*, QuBE: a qubit-controller with broadband electronics, APS March Meeting, Minneapolis, D49.00004 (2024).
- [54] C. R. Paul, Solution of the transmission-line equations under the weak-coupling assumption, *IEEE Transactions on Electromagnetic Compatibility* **44**, 413 (2002).
- [55] D. M. Pozar, *Microwave Engineering* (John Wiley & Sons, 2011).
- [56] M. H. Devoret, *Quantum Fluctuations: Les Houches, Session LXIII*, edited by S. Reynaud, E. Giacobino, and J. Zinn-Justin (Elsevier, Amsterdam, 1997) p. 351.
- [57] U. Vool and M. Devoret, Introduction to quantum electromagnetic circuits, *International Journal of Circuit Theory and Applications* **45**, 897 (2017).
- [58] A. A. Houck, J. A. Schreier, B. R. Johnson, J. M. Chow, J. Koch, J. M. Gambetta, D. I. Schuster, L. Frunzio, M. H. Devoret, S. M. Girvin, *et al.*, Controlling the spontaneous emission of a superconducting transmon qubit, *Physical Review Letters* **101**, 080502 (2008).
- [59] C. W. Gardiner and M. J. Collett, Input and output in damped quantum systems: Quantum stochastic differential equations and the master equation, *Physical Review A* **31**, 3761 (1985).
- [60] S. S. Mohan, M. del Mar Hershenson, S. P. Boyd, and T. H. Lee, Simple accurate expressions for planar spiral inductances, *IEEE Journal of Solid-State Circuits* **34**, 1419 (1999).
- [61] J. Gambetta, W. Braff, A. Wallraff, S. Girvin, and R. Schoelkopf, Protocols for optimal readout of qubits using a continuous quantum nondemolition measurement, *Physical Review A* **76**, 012325 (2007).